RADAR EVIDENCE OF SUBSURFACE LAYERS IN THE NORTHERN MID-LATITUDES OF MARS

DEVANSHI KACHOLIA
June,2022

SUPERVISORS:
W.H. Bakker, MSc
Dr.ing. H. Aghababaei

RADAR EVIDENCE OF SUBSURFACE LAYERS IN THE NORTHERN MID-LATITUDES OF MARS

DEVANSHI KACHOLIA
Enschede, The Netherlands, June,2022

Thesis submitted to the Faculty of Geo-Information Science and Earth Observation of the University of Twente in partial fulfilment of the requirements for the degree of Master of Science in Geo-information Science and Earth Observation.
Specialization: Geoinformatics (GFM)

SUPERVISORS:
W.H. Bakker, MSc
Dr.ing. H. Aghababaei

THESIS ASSESSMENT BOARD:
Dr. H.M.A van der Werff (Chair)
Dr. O. Ruesch (External Examiner, University of Münster, Germany)

Dedicated to those who lost their loved ones
in the unfortunate times of COVID-19

ABSTRACT

The topic of this study is to investigate the subsurface of glacier-like forms in the Deuteronilus Mensae region of Mars. The primary purpose of this research is to confirm or reject the presence of subsurface echoes in the debris-covered landforms using radar datasets. In the literature, landforms like lobate debris aprons and lineated valley fills are closely studied for under the surface deposits or layers. They are now considered the hub of subsurface ice in the mid-latitudes. However, smaller, and recently active glacier-like forms have not been fully explored. This research, therefore, aims to target these more minor yet significant glacier-like forms which could be the focal point for studying the Martian glacial land system. This study advances with processing the radar images and building comparisons between the original and the processed to distinguish and highlight any possible subsurface interfaces, thereby helping in locating glacier-like forms rich in subsurface deposits. With this approach, radar evidence of subsurface layers in the target glacier-like forms can be found, which would help uncover the recent climatic change on Mars. Furthermore, with the findings of this study, a better grasp of these active hydrological landforms on the Martian surface will be built, which can lead to discovering more areas of interest to further study water and ice on Mars.

ACKNOWLEDGEMENTS

I would like to show my sincere gratitude to my supervisors Wim Bakker and Hossein Aghababaei, for their insights, thought-provoking questions, and encouragement. Their constant positive attitude towards this research helped me stay confident throughout the thesis phase.
I would also like to thank Mr. Matthew Perry, Research Associate at Planetary Science Institute, Colorado, for helping me understand the SHARAD dataset better. Thanks to the CO-SHARPS team for their assistance in operating the software whenever needed. I would also like to thank Lennard Pauw, masters' student at the University of Münster, who helped me understand the geology of the study area and gave me insights into the history of the Martian surface.

A big thank you to my parents and brother for believing in me and going out of their way to always support me. My heartfelt gratitude to Vinith, who always made me feel at home and had unconditional faith in my capabilities.

I would especially like to mention my friends from India, Kareena and Shagun, for their constant support since childhood. My sincere thanks to all my friends in ITC, specially Azeb, Nimisha, and Salar, for helping me in the most stressful times of my life and being there for me throughout.

TABLE OF CONTENTS

LIST OF ABBREVIATIONS

1. **VFFs**: Viscous flow features
2. **GLFs**: Glacier-like forms
3. **LDAs**: Lobate debris aprons
4. **LVFs**: Lineated valley fills
5. **CO-SHARPS**: Colorado SHARAD Processing System
6. **SHARAD**: SHAllow RADar

LIST OF FIGURES

LIST OF TABLES

1. INTRODUCTION

In recent years, the Martian world has drawn the attention of researchers all over the globe. Mars' rich geological record and fascinating history led scientists and space organisations to be keen on studying the planet more closely. The leading purposes of several studies on the red planet include assessing the potential of harbouring life and providing resources for future human exploration (Nazari-Sharabian et al., 2020). The similarities between Mars and early Earth are a big part of why people want to study it. Little has changed on Mars since the Hesperian epoch, 2.9 billion years ago, due to the lack of plate tectonics (Victoria et al., 2018). As a result, unlike Earth, it is possible to look at Mars as a blank canvas due to no artificial structural advancements. The slightest similarity with Earth opens chapters of the history of the red planet and enables us to understand its present and past environments better.

Water is a vital ingredient for life to exist on Earth. Thus, it becomes a key element to look for to understand and develop life as we know it on Earth. Subsequently, there have been several successful Martian missions to build our knowledge of what exists on Mars in the past few decades. Mariner 9 was the first Mars orbiter to return photos of the whole planet's surface successfully. Thereby leading to the mapping of channels that resemble fluvial landforms on Earth and small valley-like structures (Rice et al., 2008), which gave us a hint of the existence of water millions of years ago on Mars. In addition to this, with Perseverance, Curiosity, and other rovers on Mars, many areas are closely studied for water-related mineralogical and geological evidence. With the discovery of geological landforms that resemble small valleys and river plains, the possibility of finding water in one or the other form on Mars has only increased (Victoria et al., 2018). Mars' glacial history discloses many drastic events that occurred and led to the formation of valleys, river plains, and glacial-like landforms (Conway et al., 2018). The presence of glacial formations on Mars from millions of years ago indicates a similarity between Mars and Earth. Because life (as we know it) requires water, the presence of these glacial formations on Mars has attracted our attention over the years which lead to studying Mars extensively.

1.1. Martian glacial history and viscous flow features

The fact that the glacial features are still visible now says volumes about the events that led to their genesis. The glacial system on Mars includes a variety of geologically intriguing landforms and are categorised by previously done studies (Baker and Head, 2015; Morgan et al., 2009; Souness et al., 2012). One set of landforms that has obtained a lot of attention are associated with processes relating to water ice and are a significant part of the glacial activity on Mars. Many of these landforms share visible similarities with terrestrial glaciers (Head et al., 2005, 2003), with a general appearance of down -slope flow and deformation (Milliken et al., 2003). These landforms also appear in elongated forms showing evidence of flow, such observations have led to the usage of the term viscous flow features or VFFs (Souness et al., 2012). Their visible 'flow' characteristics (figure 2) and abundance in the mid-latitudes can be explained by the mid-latitude glaciation hypotheses. As the VFFs are closely associated with water-ice, flow of ice is thought to be primary reasons for their formation several hundred million years ago. A study about ice accumulation on Mars (Head et al., 2005) holds the larger shift in the rotational axis of Mars accountable for the buildup of ice in the mid-latitudes. Changes in the orbital and rotational parameters have allowed ice from ice-rich polar regions to shift towards the equator (Mischna et al., 2003). In figure 1, a larger tilt leads to ice accumulation in the mid-latitudes (lower latitudes), whereas with a smaller tilt, we see ice deposits on the poles. The shifting of ice due to the changes in the tilt of the planet may have led to the formation of VFFs and this process is coined as mid-latitude glaciation (A. J. Hepburn et al., 2020; Milliken et al., 2003).

Even after millions of years to the formations of VFFs, the topic of their role in Martian glacial history is raised. The fact that the VFFs are preserved to this day is attributed to the ice being shielded from sublimation by surface debris (Holt et al., 2008). The onset of the collapse of ice sheets in the ice accumalated regions (mid-latitude glaciation) resulted in exposure of underlying debris. This created a barrier and slowed down the sublimation process (Dickson et al., 2008). The existence of VFFs till present day can thus be explained by this deglaciation process closely modelled by (Fastook et al., 2014). Ice flow from the poles to the mid-latitudes and subsequent deglaciation is believed to have led to the existence of buried ice deposits in the mid-latitudes (Head et al., 2005). The VFFs are the hub of glacial deposits (Petersen et al., 2018) and therefore are the ideal features to look for any signs of water. Further examination of these features and their underlying deposits may yield information on Mars's historical climate and the events that have manifested in significant geographical and climatic changes. A few researchers have thoroughly studied these landforms for hydrous minerals and under the debris deposits described in section 1.2.

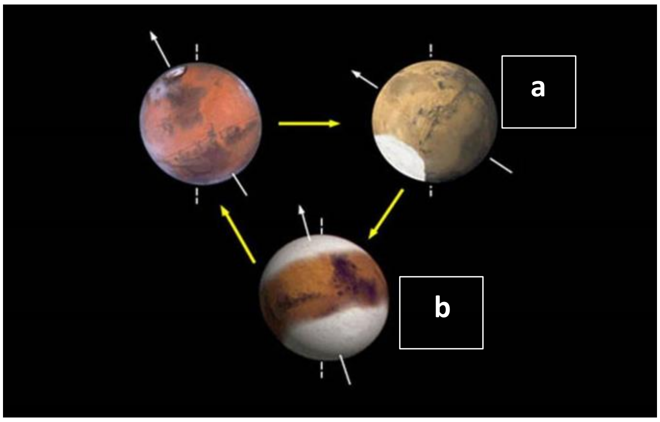

Figure 1: Ice tends to be in the mid-latitudes (a) when the tilt is larger. When the tilt is low (b), ice accumulates at the poles (NASA/JPL-Caltech, 2018).

1.2. State of the art

In previous studies, radar datasets are used to look for subsurface deposits under several viscous flow features. The term 'viscous flow feature' or 'VFF' can be used for all glacial type formations, which demonstrate the proof of viscous flow (Souness et al., 2012). All the glacial type landforms that have formed in the last several hundred million years ago due to mid-latitude glaciation can come under the VFFs category (A. J. Hepburn et al., 2020). VFFs are abundant on Mars and also include Lineated valley fills and concentric crater fills (Levy et al., 2014).

Radar imagery have been taken advantage of for studying subsurface ice deposits both in the mid-latitudes and ice bearing polar regions on Mars. The Martian poles are known for bulk deposits of ice in their subsurface. The north polar layered deposits are considered to be the largest reservoir of water ice on Mars (Lalich et al., 2019). The polar deposits are studied thoroughly for age, volumes and, physical properties of ice deposits and have detected a bulk of layers underneath the surface (Head et al., 2003; Lalich et al., 2019; Smith et al., 2021, 2016). Apart from polar regions, the Martian subsurface is also studied for ice deposits in northern and southern mid-latitudes (Holt et al., 2008; Morgan et al., 2021). There are many VFF rich areas on Mars closely studied for subsurface deposits through radar sounding which led to detection of subsurface interfaces under VFFs in Arcadia Planitia and Utopia Planitia (Bramson et al., 2021, 2015). Additionally, the entire belt of north-east lowlands that covers Deuteronilus Mensae, Protinilus Mensae and Nili Fossae are VFF rich areas which are also observed using geomorphological evidence and Context Camera imagery (A. J. Hepburn et al., 2020; Souness et al., 2012).

The VFFs exist in various forms and sizes as shown in figure 2. There are lineated valley fills (LVF) which are the highest order of VFFs as they extend for several kilometers followed by lobate debris aprons (LDA). The lowest order of VFFs are called glacier-like forms (GLFs) as they extend for less than 5 km and usually fuel the larger valley fills marked with arrows in figure 2 (A. J. Hepburn et al., 2020). GLFs can be distinguished from apron-like LDAs based on their length to width ratio. The length of the GLFs must be longer than the width therefore the ration must be greater than 1. They can also be distinguished by differences in color, texture, and down-slope flow from the surrounding terrain. In Souness study (2012), condition to demarcate the GLFs is described in detail. Depicted in the figure 2 below are small alcoves called as GLFs which are feeding the larger order landforms called LVFs.

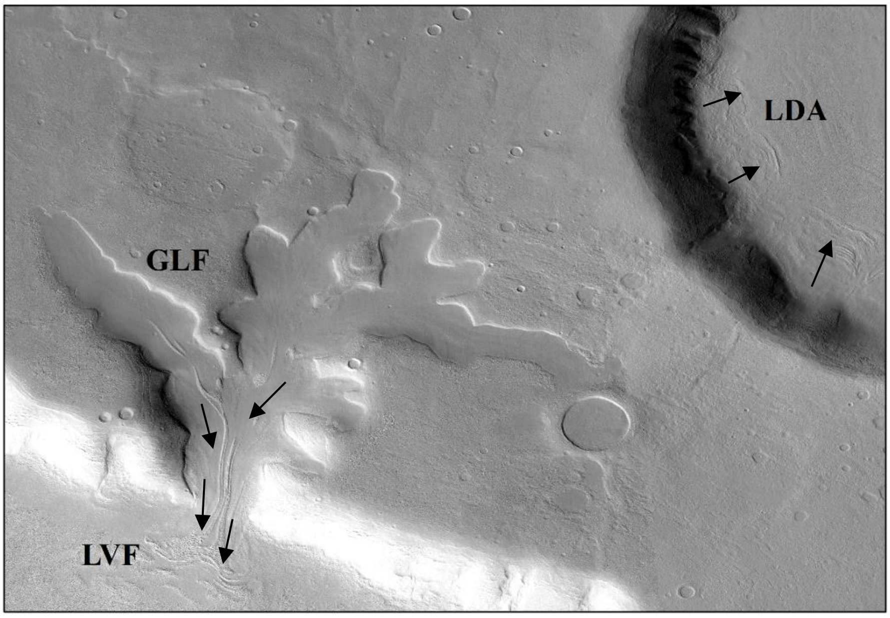

Figure 2: Glacier-like forms fuelling the lineated valley fills in a small are in Deuteronilus Mensae. All the features are showing viscous flow marked with arrows. Base imagery: Murray Lab CTX mosaic. The image has illumination from the bottom; therefore, the feature would appear elevated. They are generally depressed and at a slope.

In the literature the nomenclature used for GLFs varies including small scale LVF (Levy et al., 2007), glacier-like flows and superposed lineated valley fill (Levy et al., 2007). As described by (Head et al., 2010) and shown in figure 3 GLFs typically flow into pre-existing VFFs to form Mars' integrated glacial land system as described by (Head et al., 2010). The GLFs correspond to a more recent and small-scale glacial phase, on the other hand the larger VFFs like LDA and LVF deposits record an earlier glacial phase (Brough et al., 2019; Dickson et al., 2008; Levy et al., 2007). The larger scale landforms such as LDA are studied for ice deposits underneath the debris using radar datasets (Jeffrey J Plaut et al., 2009) and are considered to be the hub of glacial deposits. With the help of SHAllow RADar (SHARAD) instrument's radar imagery, LDAs in the mid-latitudes have shown the evidence of under the surface or subsurface ice layers (Bramson et al., 2015; Head et al., 2010; Holt et al., 2008; Stuurman et al., 2016).

However, the more recent and small-scale landforms such as GLFs (Brough et al., 2019) still need to be looked at for any evidence of deposits underneath the debris. There are limited studies that focus on the GLFs and their formation over the years (Degenhardt and Giardino, 2003; Holt et al., 2008; Karlsson et al., 2015; Souness et al., 2012). There have been attempts to date these viscous flow features by examining their composition (A. J. Hepburn et al., 2020) that have led to some progress in interpreting the glacial history of Mars through these landforms. Though, there is still a lack of knowledge of the depths of the GLFs and how these VFFs are different from each other. The grounds for the absence or presence of ice layers under these landforms have not been explored in full detail. With exploring the GLFs, the grasp on the causes of their formation and the climatic changes that impacted them is built. GLFs are significant as they are the highest altitude constituent of the Martian glacial valley system (Brough et al., 2019). They might serve as a focal point for studying Martian glacial activity because of their size and shape resemblance to terrestrial glaciers (Conway et al., 2018). The subsurface of these small-scale landforms has yet to be thoroughly investigated for any signs of glacial activity on Mars several million years ago, such as layers, deposits, or ice. The depths of the GLFs may be archives of recent climatic changes on Mars and with radar imagery better grasp can be built on these recently active hydrological landforms. To bridge the gap of uncertainty among these landforms, this study seeks to analyze the subsurface of GLFs using radar imaging to acquire an overview of the prevalent absence or presence of subsurface deposits.

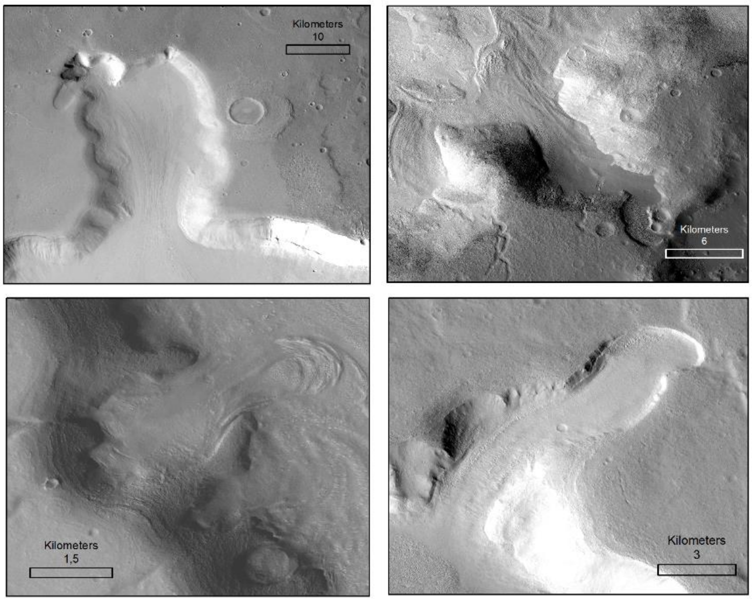

Figure 3: Lineation and flow-like pattern visible on a few GLFs present in the Deuteronilus Mensae region. They are confined to valleys/depressions and on average are ~4 km long and ~1 km wide (Souness et al., 2012).

1.3. Research objectives and questions

Observing glacier-like forms for subsurface layers using SHARAD data in the Martian mid-latitudes. This study proceeds with the selection of a few target landforms to understand the implication of the glacial history of Mars on the GLFs.

1.3.1. Research objectives

1. To determine if ice layer deposits exist under the GLFs and possibly identify them using a limited number of classification methods.
2. To quantitatively assess the method and algorithms utilized to locate ice layer deposits.
3. To judge the effectiveness of SHARAD-radar dataset in detecting ice layers.
4. To study the surface composition of the ice-rich and non-ice-rich GLFs in the mid-latitudes.

1.3.2. Research questions

a) Which of the GLFs are suitable targets for studying ice layers?
b) How can ice layers be detected under these landforms using radar imagery?
c) Are there ice layers present under the GLFs in the Mid-latitudes?
d) Which target landforms seem to be richer in ice deposits?
e) Which of the chosen methods seem suitable for detecting ice using radar imagery?
f) How different is the surface composition of ice rich GLFs from the GLFs with relatively few or no layers?

The original research questions were modified from the research proposal and were narrowed down as the study progressed. Reasons for the modifications are stated in chapter 5.

2. DATASET AND STUDY AREA

Any subsurface deposits whether ice deposits or layers will most likely exist on Mars in the form of dust and dirt mixture (Dundas et al., 2018). Hence observing it using optical imagery is not easy due to the inability of the signal to penetrate the dust and debris and subsequently look for under the surface deposits. Penetration through the surface layer is vital to explore the subsurface of the debris-covered glacier-like forms. Unlike the short wavelengths used on Earth for monitoring areas with low to moderate penetration, change detection, etc., a very long wavelength is used on Mars for better penetration of signals into the target landforms. The Shallow Radar (SHARAD) instrument is a subsurface-sounding radar present onboard NASA's mission Mars Reconnaissance Orbiter and was developed by the Italian Space Agency (ASI). It produces very long wavelength radar imagery and can be utilized to detect subsurface interfaces on Mars. SHARAD operates with a 20-MHz center frequency and a 10-MHz bandwidth, resulting in a vertical resolution of 15 m in free-space and $15/\sqrt{\varepsilon}$ m in a medium of relative permittivity ε. The transmitted signal is a 85-μsec chirped pulse emitted from a 10-m-long dipole antenna that can be used for both transmitting and broadcasting (Seu et al., 2007). Like Earth, the transmitted signal to Mars' surface is frequency modulated (chirp) to achieve effective pulse lengths and better time/ distance resolution (Seu et al., 2007).
The radar sends high-power pulses through the antenna towards the Martian surface which operate between 15-25 MHz frequencies and can reach up to 1 km (Seu et al., 2004). The main objective of SHARAD is to map di-electric interfaces to a few hundred meters depth and thus enable the interpretation of these results in terms of the distribution of expected materials. Horizontal surface resolution of SHARAD is dependent on the surface roughness, but for surfaces on Mars, the cross-track footprint is 3-6 km, and the along track footprint is 0.3-1 km (Seu et al., 2007). The system characteristics and operational details of SHARAD can be seen in figure 4, taken from the study by Vanshika Gupta (2020). The specifications at which the instrument operates are listed in table 1.
SHARAD has penetrated through the kilometer-thick north and south polar layer deposits and has been able to detect many internal reflectors (Campbell and Morgan, 2018; Holt et al., 2008). Thus, with SHARAD's signal, penetration through the debris over the GLFs is possible and would be effective to yield a view of the subsurface of the target areas.

Parameters	SHARAD
Frequency band	15-25 MHz chirp
Vertical resolution in free space	15 m
Transmitter power	10 W
Pulse length	85 μsec
Antenna	10-m tip to tip dipole
Horizontal resolution	0.3-1 km x 3-6 km
Penetration Depth	~ 1 km

Table 1 SHARAD specifications

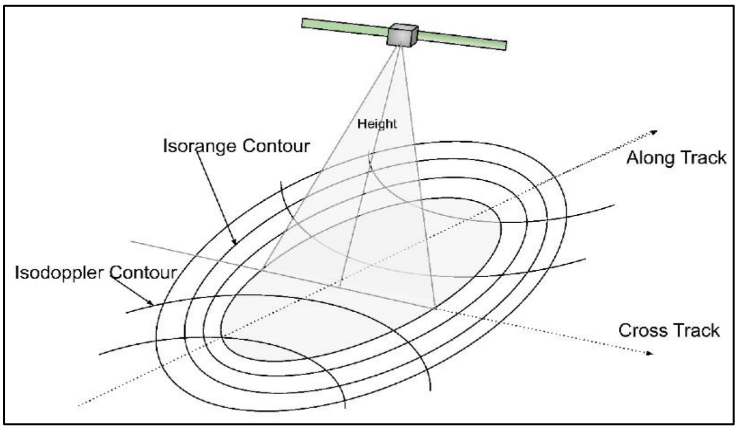

Figure 4: Concept of SHARAD's operation. Ground resolution is calculated using the cross-track range to surface distance and the doppler shift of the returning signal along the track.

2.1. SHARAD radargrams

The data obtained by SHARAD was in the form of radargrams, as shown in figure 5a, which can be found in the Planetary Data System portal (Campbell et al., 2006) used for geospatial analysis. The radargrams represent power returned at several time delays in the Y axis and along the track distance travelled by spacecraft is represented in the X-axis, figure 5a (Bramson and Petersen, 2020). The round-trip delay samples in the vertical axis are uniform at 0.0375 microseconds per pixel. Figure 5b shows a radargram and its respective track 39752.

SHARAD radargram files are obtained from the PDS archive. Each radargram file is a 32-bit floating-point format accompanied by a TIFF image. For this study, TIFF images are utilized, which logarithmically scales the backscatter power over an 8-bit range corresponding from -3dB to +32 dB with respect to the background (Campbell, 2014). Each DN step is about 0.137 dB. It is possible that a few of the radar observations might appear brighter than the others. The inconsistency maybe arising due to the lower scaling factor used in the processing stages before publishing the data. Tracks collected before or around 7200 possibly contain more background noise; due to the use of a lower scaling factor, the TIFF radargram products appear slightly brighter (Campbell, 2014).

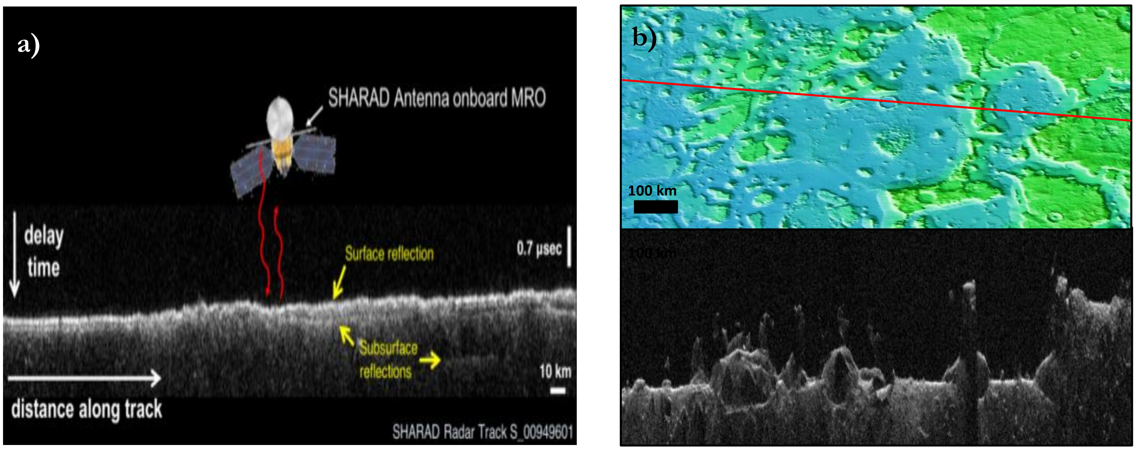

Figure 5: a) SHARAD radargram representing time delays in Y-axis and distance along track in X-axis (Bramson and Petersen, 2020). b) Track of radargram S_03975201 is shown in the red line on Mars Orbital Laser Altimeter DEM along with the radargram representing power backscatter received from the areas in the path of the track.

While the instrument tracks the surface, the first observed echo is the strong return from the surface, which loses its strength with time delay. As the reflecting interface's depth grows, the subsurface's signal intensity typically falls until the signals are lost due to a combination of surface clutter or cosmic radio noise (Seu et al., 2007). Clutter or unwanted signals can become a hurdle while studying target landforms for the presence of any subsurface interfaces. Interference from off-nadir surface echoes is the main stumbling block to identifying subsurface reflections. At longer time delays, the echoes from topographic features away from the nadir track arrive at the same time as the subsurface echoes and add undesired 'clutter' power as shown in the schematic figure 6 taken from (Mishra and Bharti, 2020). This issue can be recognized and mitigated through a few methods discussed in section 3-methodology.

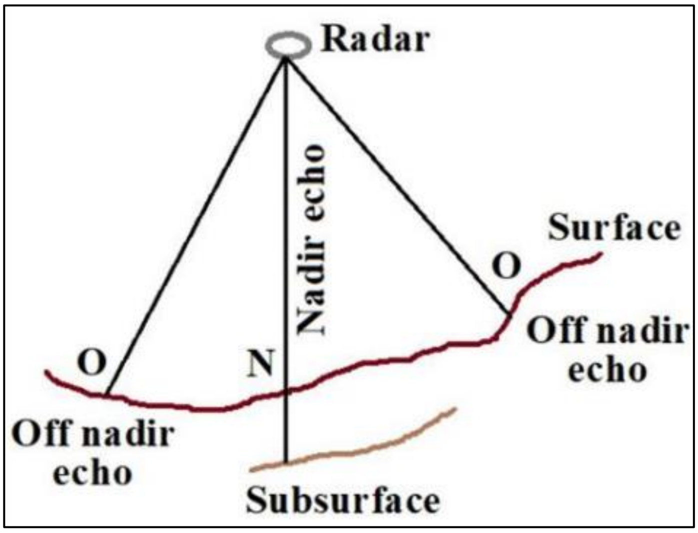

Figure 6: Schematic of generation off-nadir surface echoes resulting in unwanted noise or 'clutter'. Schematic taken from (Mishra and Bharti, 2020)

2.2. Study area

As stated earlier, GLFs are distributed all over Mars. Interestingly, studies have found that the latitudinal range of GLFs exhibits hemispheric symmetry since both the northern and southern lowlands are rich in viscous flow features. The location of these features in the mid-latitudes strongly supports the mid-latitude glaciation process known to have occurred during the late Amazonian period.
There are 1243 GLFs on the red planet, as delineated by Souness and Brough (Brough et al., 2019; Souness et al., 2012). The majority of the GLFs are present in the northern lowlands, as illustrated in figure 7a. Especially the Deuteronilus Mensae, Protinilus Mensae, and Nilosyrtis Mensae belt at the northeastern mid-latitudes account for 509 of the total GLFs on Mars.

2.2.1. Geological context of Deuteronilus Mensae

Located south of the Lyot crater (50.46º N, 29.31º E) is a region of mesas called Deuteronilus Mensae. Lineated valley fills and lobate debris aprons are prevalent in this region and are considered to have developed due to glaciation in the Late Amazonian period (Dickson et al., 2008; J J Plaut et al., 2009). Due to their fluvial character, the massive subsurface ice deposits observed using SHARAD radargrams in this region are strongly correlated with LDAs and LVFs. (Morgan et al., 2009). Deuteronilus Mensae consists of a widespread presence of features contributing to the glacial land system of Mars. With the presence of LVFs and LDAs in this region, the emergence of lower-order alcove GLFs, which feed more extensive forms, is expected.
As per the delineation of GLFs done by previous studies (Brough et al., 2019; Souness et al., 2012), out of the 509 GLFs present in the northeastern lowlands around 127 are found in the Deuteronilus Mensae region. The global distribution of GLF is shown in the map in figure 7a taken from the study by Souness (2012).
Deuteronilus Mensae is topographically dense and bears dramatic features all along its terrain. For this study, a small terrain was selected where total 23 GLFs are present in extremely small and large sizes, depicted in figure 7b. The GLFs present in the area will be studied for any sign of subsurface interfaces using SHARAD radargrams.

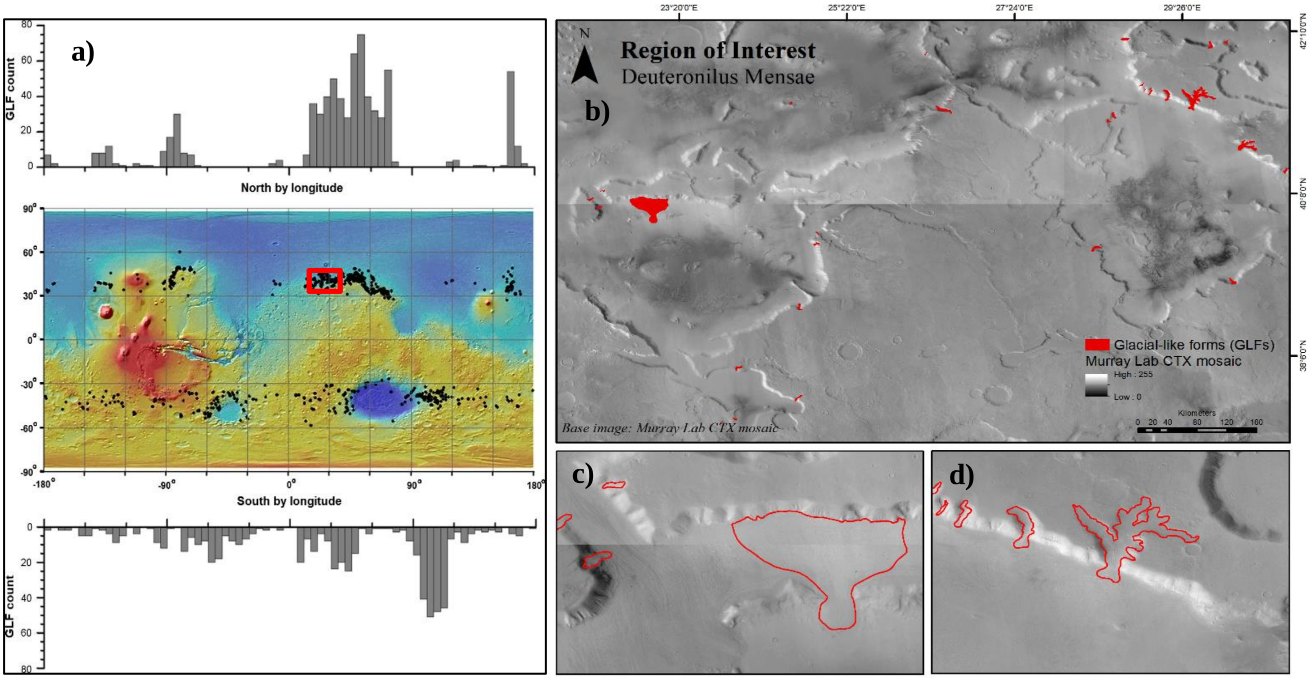

Figure 7: a) Global distribution of 1243 GLFs on Mars. Majority of the GLFs shown in black dots are in the northern lowlands. Small area marked in red is Deuteronilus Mensae. Image source: (Souness et al., 2012). b) A section of Deuteronilus Mensae is taken to study the GLFs in this area. c) and d) shows the zoomed in view of the GLFs in the selected area. The delineated GLFs are obtained from the study by (Brough et al., 2019).

3. METHODOLOGY

The main aim of this research is to recognize the subsurface echoes and subsequently broaden our knowledge of the small-scale landforms. Methods chosen to advance this study involve selecting and processing the data for our area of interest. Furthermore, we utilize other helpful Martian datasets to examine the landforms for any hydrological remains.
The following sections are divided mainly into three categories 1) Looking for target landforms based on mineralogical evidence 2) obtaining radargrams, and 3) Performing clutter simulations on the selected radargrams.

3.1. Target glacier-like forms

Mid-latitude glaciation hypotheses suggest that VFFs are the hub of glacial deposits, which is primarily supported by the ice layers detection under LVFs and LDAs in previous studies. Correspondingly, the scattered GLFs in the chosen area could be the potential hubs of glacial deposits due to the mid-latitude glaciation process.
The GLFs are dispersed in the region and come in various shapes and sizes, it is likely that a few GLFs are more promising than others for subsurface deposits. Before promptly processing the radargrams covering all the GLFs, a selection process was conducted by utilizing the products from the Compact Reconnaissance Imaging Spectrometer or CRISM. The following step in sub-section 3.1.1 seeks to look for a few target GLFs for this study and to further analyze the radargrams.

3.1.1. Observing glacier-like forms for hydrous minerals using CRISM data

It is now evident that GLFs in the designated area might represent possible centers of glacial deposits. Due to the glacial history of the landforms and the notion of an ocean existing on Mars billions of years ago, it is likely that the GLFs show evidence of hydrous/aqueous minerals.
Among the many instruments mounted on Mars Reconnaissance Orbiter (MRO), one which aims to map the minerology of Mars is Compact Reconnaissance Imaging Spectrometer or CRISM (Murchie, 2010). CRISM is a hyperspectral imager that collects visible/shortwave-infrared wavelength reflectance data from two detectors with wavelengths ranging from 0.36 to 3.92 micrometer (Murchie et al., 2007). The primary objective of this instrument is to map the Martian surface using spectral bands and study the minerals. It was developed to map the mineralogy of key areas at a highest spatial resolution of 15-19 m/pixel. There are summary products also publicly available which were already characterized by the known diversity of minerals on Mars. Summary products are a set of 60 spectral characteristics obtained from corrected spectral reflectance at key wavelengths in CRISM targeted observations (Viviano-Beck et al., 2014). Prior to looking at these potential-layer bearing landforms for any subsurface deposits, we looked at the CRISM summary products for any signs of hydrated minerals, hydrated silica, and phyllosilicates in the selected area. These minerals are categorized, and their presence can be seen based on the indices the images represent.
CRISM images are observed for hydrous minerals, hydrated silica, phyllosilicates, and Iron (Fe) and Magnesium (Mg) phyllosilicates using QGIS 3.16 program. The following figure 8 shows the footprints of CRISM images in the selected region of Deuteronilus Mensae, which are observed for the above-mentioned minerals and will be discussed in detail in the next chapter. All the product IDs used in the map are listed in table 2. In addition, observing the area for any evidence of hydration could give us a hint of key areas to study further using SHARAD data.

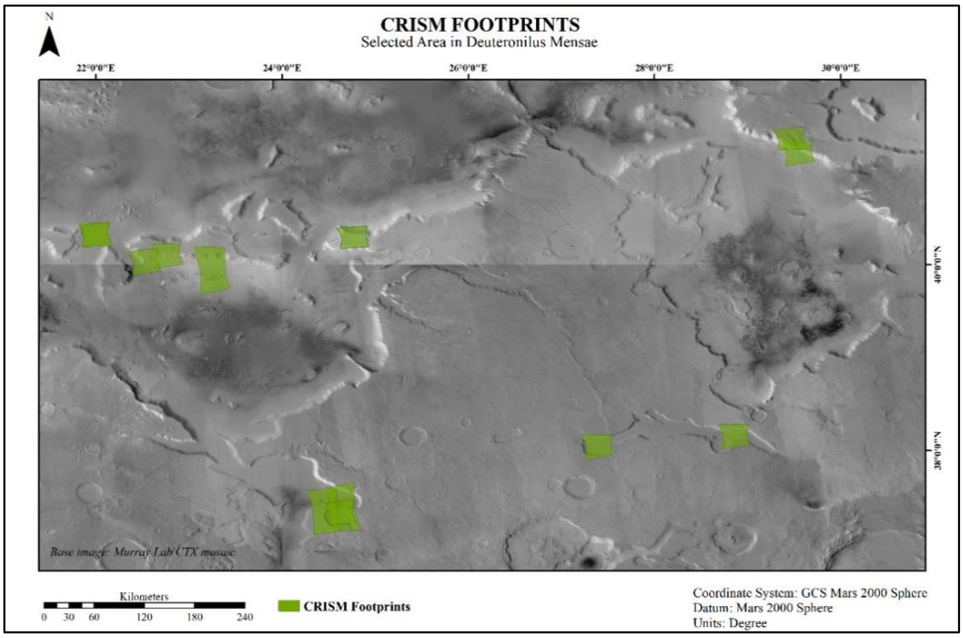

Figure 8: CRISM footprints present in the selected area of Deuteronilus Mensae. Base image: Murray Lab CTX mosaic.

CRISM Products IDs visible on the map (figure 8)	
HRL0000BEF4_07_IF184J_MTR3	FRT000090A0_07_IF167J_MTR3
FRT000049FF_07_IF167J_MTR3	FRT0000A230_07_IF167J_MTR3
FRT00013F15_07_IF167J_MTR3	FRT0000A230_07_IF167J_MTR3
HRL0000AB4C_07_IF184J_MTR3	FRT000109A8_07_IF167J_MTR3
HRL0000C001_07_IF184J_MTR3	FRT0001682D_07_IF167J_MTR3
FRT00008780_07_IF167J_MTR3	FRT00016D34_07_IF167J_MTR3
FRT00009486_07_IF167J_MTR3	FRT000098A6_07_IF167J_MTR3

Table 2 CRISM Product IDs. Footprints of these product IDs are shown on the map of figure 8.

3.2. Selection of SHARAD radargrams

To proceed with the processing and analysis of radargrams, the appropriate collection of data must be acquired first. Consequently, the SHARAD tracks for the target regions are identified by inspecting track locations/coverage available at the planetary data archive returned from NASA's planetary missions (PDS). One site in the ROI along with SHARAD stamps in the area, are shown in figure 9. It should be noted that the image only displays a few tracks for the specified location. After identifying the coverage of the tracks, the radargrams of interest are downloaded. Post identifying the IDs of the radargrams, Java Mission-planning and Analysis for Remote Sensing or JMARS can be used to enter the IDs and study the radargrams directly. JMARS is a geoinformation system developed by Arizona State University which allows data analysis and is employed for this step (Adler et al., 2016). The coverage and position of the radargram was easily determined using JMARS, which also allows overlaying of the SHARAD tracks on several Martian orbital datasets.

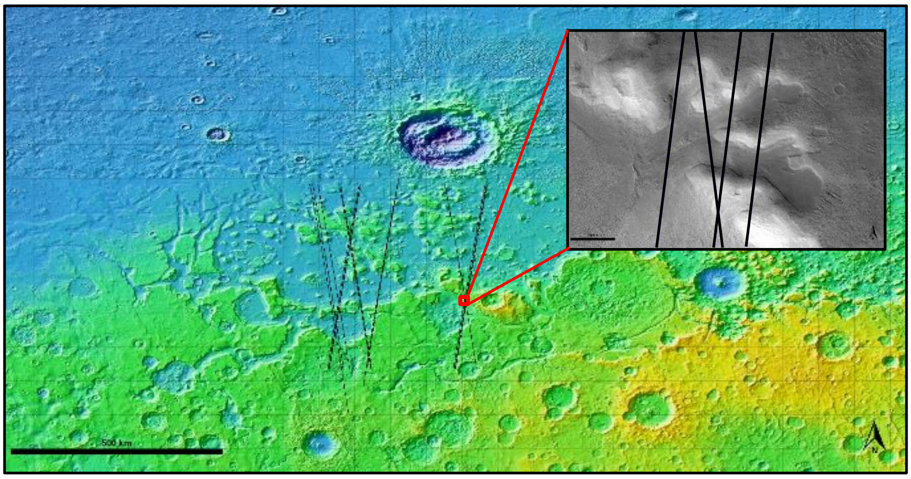

Figure 9: Selected track locations of the radargrams in the designated area. In the small window is a zoomed in view of the tracks chosen over a GLF. Base images: Coloured map-MOLA colourized elevation, small window- Dynamic Mix of MOLA, THEMIS, and CTX Global mosaics from JMARS.

3.3. Clutter simulations

The processing technique for the selected radargrams from the previous phase is described in depth in this section. The selected radargrams are processed in this stage, and processing of a planetary datasets like SHARAD comes with a set of challenges. Pre-processing data, instrumentation complications, untimely signal loss, and so on are a few of the issues that come with processing and pre-processing planetary datasets. Since this research focuses on recognizing subsurface echoes, dealing with, and distinguishing off-nadir echoes was a major challenge. As stated in section 2.1, with radar imagery comes the issue of off-nadir reflections, which are frequently misinterpreted for echoes from the subsurface and hinders the possibility of making a reasonable observation. Thus, it is vital to comprehend the origin of the unwanted echoes to address them later.

Off-nadir reflections can be defined as echoes coming from topographical features located away from the nadir track. Especially at longer time delays when the off-nadir reflections happened to arrive at the same time as the reflections from the subsurface, they are misinterpreted as subsurface echoes. The echoes in the radargram appear to be arising from the subsurface, but it is likely that those signals are from features far away from the nadir track. These off-nadir reflections, also known as 'clutter' is undesired and build difficulty while observing the radargrams for subsurface echoes.

3.3.1. Colorado Shallow Radar Processing System

To help differentiate between clutter and subsurface echoes, the SHARAD team designed a processing system. Colorado Shallow Radar Processing System is a boutique that allows generating clutter simulations and depth-correcting the radargrams using a fixed set of parameters (Putzig, 2014). Clutter simulations show a predicted signal in the absence of subsurface reflectors. These simulations illustrate the surface clutter and off-nadir reflections of the radargrams and thus can be used to eradicate the challenge of misinterpretation of the origin of signals.

The clutter simulator in the CO-SHARPS boutique generates clutter grams which can be identified with the key name QDA and operate on Jet Propulsion Laboratory (JPL) focused processor (Gupta et al., 2020). The QDA products are simulated using the digital elevation model obtained from the Mars Orbital Laser Altimeter (MOLA) of ~463 m resolution (Smith, 1999).

After identifying the product IDs of the radargrams over the target areas, the boutique was employed to generate clutter simulations. The simulator allows adjusting a fixed set of parameters. The parameters chosen for this step are as follows. Aperture (frames) are fixed in the case of QDA processor to 4096. A Hann weighting window to suppress the sidelobes, presum value 16, and fractional doppler bandwidth 0.5 are selected parameters to generate clutter simulations. In table 3, a set of adjustable and default parameters for QDA processer are listed. A custom set of parameters are chosen to enhance local features; Hann window showed optimal results compared to the Uniform weighting window, wherein a high loss of signals was observed.

Additionally, the output images were less distorted when the fractional doppler bandwidth value was reduced from default value 1 to 0.5. The weighting windows mentioned exchange better range resolution for lower sidelobe power. The default window type is a Hann window, widely employed to provide good range sidelobe reduction with slight resolution smearing.

Parameters	QDA (defaults in **bold**)	QDA chosen
Aperture (frames)	**4096**	4096
Range-compression Weighting	Uniform, **Hann**	Hann
Peak SNR in PNG (dB)	**30**	30
Focusing Method	**Omega-K, multilook**	Omega-K, multilook
Multilook bandwidth	**15**	15
Fractional Doppler bandwidth	0.25-**1.0**	0.5
Total presum	8-64 (**32**)	16

Table 3. Adjustable parameters for clutter simulator in the CO-SHARPS boutique. In ***bold*** *are default parameters that can be customised considering local features in the radargrams (Putzig, 2014). Rows shaded in blue are fixed parameters under QDA and cannot be changed. Column three lists the customized parameters selected to process the radargrams for this step.*

CO-SHARPS boutique also allows conversion of time-domain radargrams to depth corrected ones when a di-electric constant is specified. For several studies, a di-electric constant of ~3.0 -3.15 is used signifying the composition of water ice (Parsons and Holt, 2016; Whitten et al., 2017). It is important to note that in the clutter simulator, the di-electric constant is assumed to be homogeneous throughout the whole subsurface for ease of processing (Gupta et al., 2020). However, time-domain radargrams were employed in this study, and no depth correction was performed.

The simulator processes the radargrams in accordance with the parameter values entered and provided outputs. The portable network graphics (PNG) formatted results can be downloaded from the boutique as the processing is finished. The clutter simulations were viewed and compared with original radargrams using ENVI version 5.6 and GNU image manipulation program (GIMP). Both the original and processed radargrams can viewed in figure 10.

Clutter simulations obtained from the simulator are essential to build a comparison with the original radargrams. Because the simulations do not display any reflectors at depth (i.e., they show surface clutter and off-nadir reflections), they may be used to distinguish off-nadir reflections from subsurface echoes.

Along with clutter simulations, depth plots can be generated in JMARS, which plots the pixel depth and pixel values. Since the power backscatter received from the radargram is high for subsurface echoes and lower for noise, the pixel values could help differentiate between the two. This is further discussed in chapter 5.

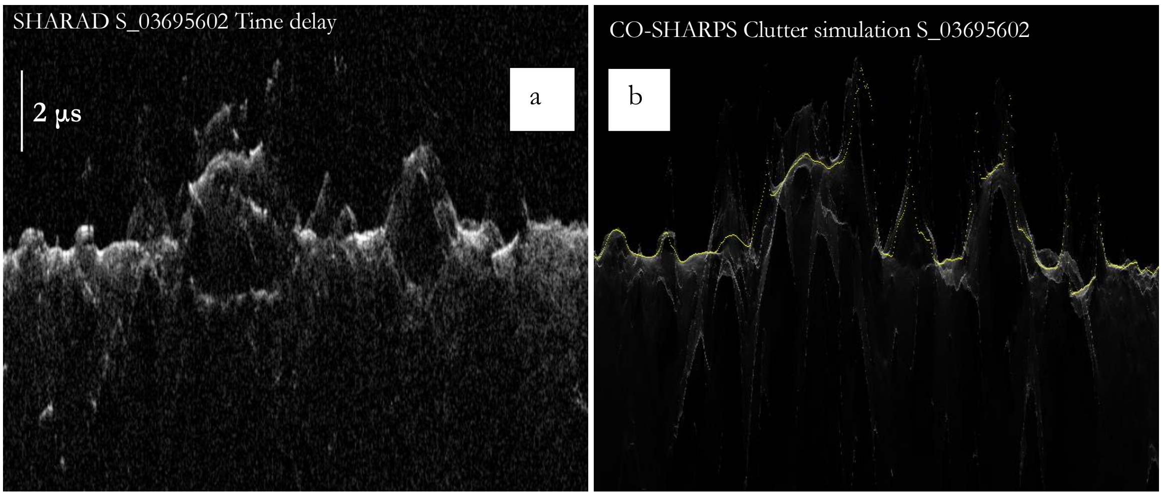

Figure 10: Images of original radargrams and clutter simulations. a) A section of the original radargram S_03695602 is shown in the image. b) Clutter simulation of the original radargram (a) simulated using CO-SHARPS boutique and selected parameters in table 1.

4. RESULTS

The methodology includes explanations for the selection of radargrams, the use of the clutter simulator, and the criteria for selecting GLFs. This chapter discusses the results from the steps of methodology and observations in detail.

4.1. Target GLFs

In the following subsections, results from the CRISM images and the selection of the GLFs are illustrated and explained.

4.1.1. Mineralogical evidence of GLFs

The decision to use CRISM images to seek evidence of hydrous minerals led to the investigation of CRISM footprints shown in figure 11. Among the many summary products available on the PDS platform, four kinds of products that represent reflectance from water bond minerals were chosen. *Hydrated minerals, hydrated silica, phyllosilicates, and phyllosilicates with Fe and Mg*- summary products were examined for any evidence of hydrous remains in the area. Figure 11 shows the close-up of products describing hydrated minerals, i.e., SINDEX2, BD2100_2, BD1900_2 is demonstrated. Hydrated minerals are comprised of polyhydrated sulphates which appear magenta in 1.9 µm and 2.4 µm absorption bands. They are also comprised of monohydrated sulphates that show yellow/green color because of strong 2.1 µm absorption and a weak 2.4 µm absorption band (Viviano-Beck et al., 2014).

Among the 23 GLFs present in the area shown in the map below (figure 11), there are only four sites where CRISM images cover the GLFs in the study area. Images that overlap the GLFs at the four sites shown in figure 11a (colored boxes) were observed for any evidence of hydrated minerals. Along with the summary products of hydrated minerals, I also looked at products of Fe and Mg phyllosilicates related to the cation composition of hydroxylated minerals. From the figures 11b and 11c only faint appearances of hydrous and hydroxylated water bonds can be identified in one region. As shown in the figure 11c different colors are visible in the Fe and Mg summary product i.e., BD2555, D2300, BD2290 RGB components which indicate the composition of hydroxylated minerals. In the Fe and Mg phyllosilicates products red/yellow colours indicate the presence of prehnite, chlorite, epidote, or Ca/Fe carbonate, while cyan colours indicate the presence of Fe/Mg smectites or Mg carbonate (Viviano-Beck et al., 2014). The exact location of the mineral indication is marked with the arrow in figures 11b and 11c. However, it can be noticed that they are in insignificant proportions and most likely could be due to noise generated in the process of acquiring and processing the data. Usually where there are significant mineral deposits, a clear pattern is seen in the CRISM data, as shown in figure 12. The example in figure 12 is from a different area. For the chosen area in this study, no noticeable patterns in the summary products of hydrated minerals, hydrated silica, and phyllosilicates were found; only faint and scattered signs of Fe and Mg phyllosilicates can be seen in figures 11b and 11c.

In the following sub-section, the selected target GLFs are described.

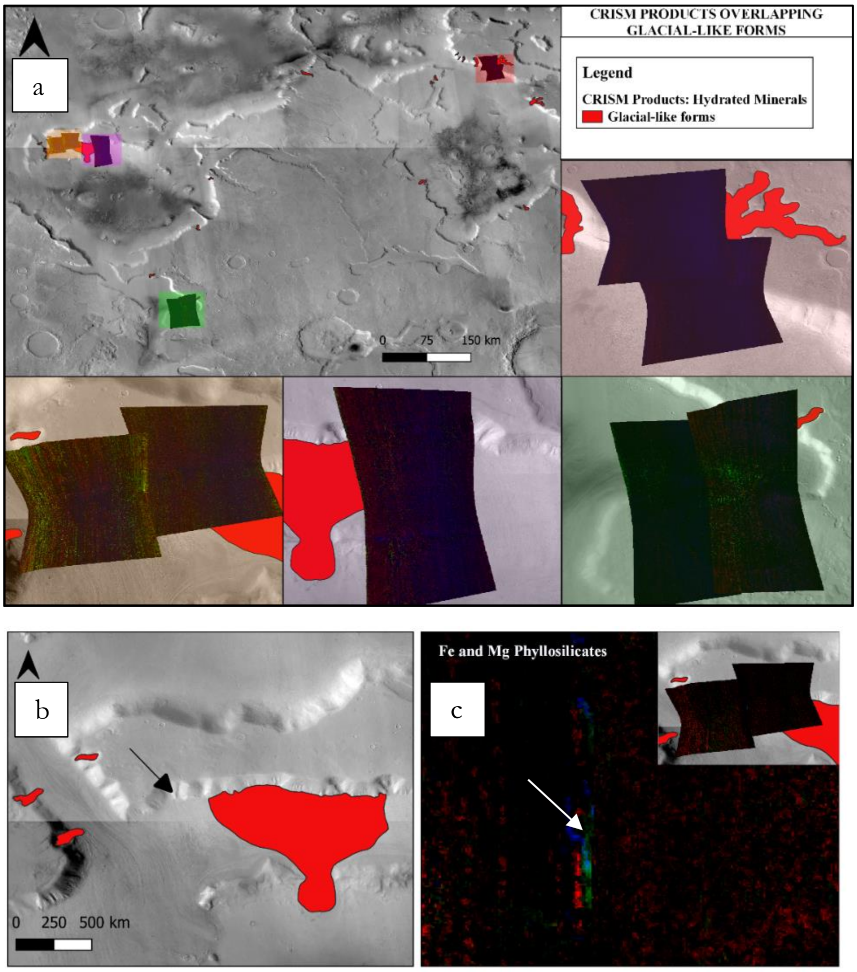

Figure 11: CRISM products overlapping glacial-like forms. a) The windows show the sites where the images are overlapping GLFs. No significant evidence of hydrated minerals identified. b) Result of the Fe and Mg phyllosilicate product for the site marked in the window. The arrow pointing out the location in b) and c) where some indication of cyan and blue is visible.

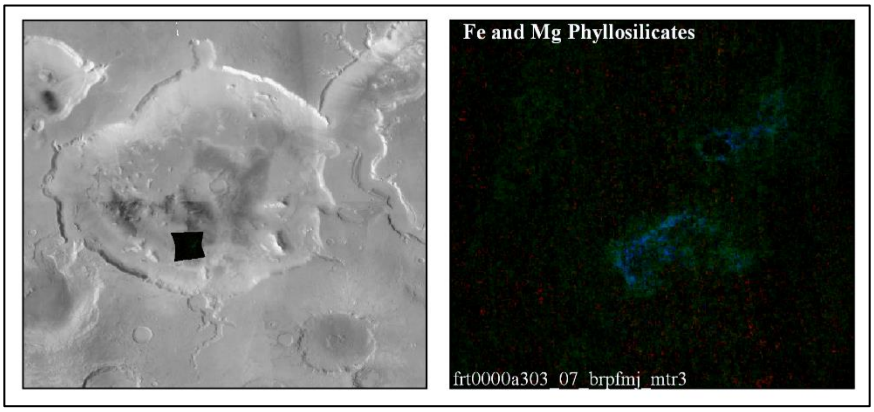

Figure 12: Example of significant mineral deposits. Fe and Mg phyllosilicates found in an area in Deuteronilus Mensae. It should be noted that this area is different from the study region and is an example to better understand the CRISM images investigated for this research. CRISM image: FRT0000A303_07_BRPFMJ_MTR3

4.1.2. Selection of GLFs

Glacier-like forms are known to stretch only for a few kilometers and are usually not more than 1 km wide. The GLFs in the study region have an average area of about 19 km². From the graph (figure 13), it can be seen that only a small number of GLFs have an area greater than the average of all the 23 GLFs. Equal distribution can be noticed for GLFs covering less or equal to 5 km² and GLFs with an area greater than 5 and less than 19 km². With this level of coverage, it was challenging to study them through SHARAD due to its broad antenna pattern, which results in surface reflections up to a few tens of kilometers away from the suborbital point in rocky areas and a few kilometers for smooth surfaces (Holt et al., 2008).

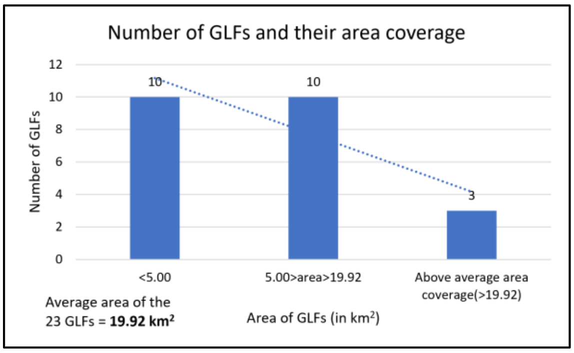

Figure 13: Graph showing the number GLFs based on their area. Area in km²

Observing the radargrams and processing them with focus on such small GLFs will be even more challenging. Therefore, to ease and assist the processing and analysis, a few larger target GLFs are selected with above-average area coverage due to the resolution of SHARAD data.

Among the 23 GLFs located in the area, three landforms are significantly larger in size than others. The GLFs of sites 1, 2, and 3, as marked in figure 14, cover 212.8 km², 90.3 km², and 39.5 km², respectively, while others range from 0.8-16 km². The three selected sites can be viewed in figure 14 (b,c, and d); site 1 is the largest of the three and show flow-like patterns. Since the figures are zoomed in, the GLFs might appear larger, but Site 2 and 3 (figures 14c and 14d) are significantly smaller than site 1 and show lineation flowing into LVFs. These observations about the area coverage and patterns are similar to how research describes GLFs, also discussed in detail in section 1.1. Observing targets larger in size helps in dealing with the resolution constraints of SHARAD data, and thus the larger sites among the 23 in the study are chosen for further processing. Listed in the table 2 are SHARAD radargram IDs selected for each site.

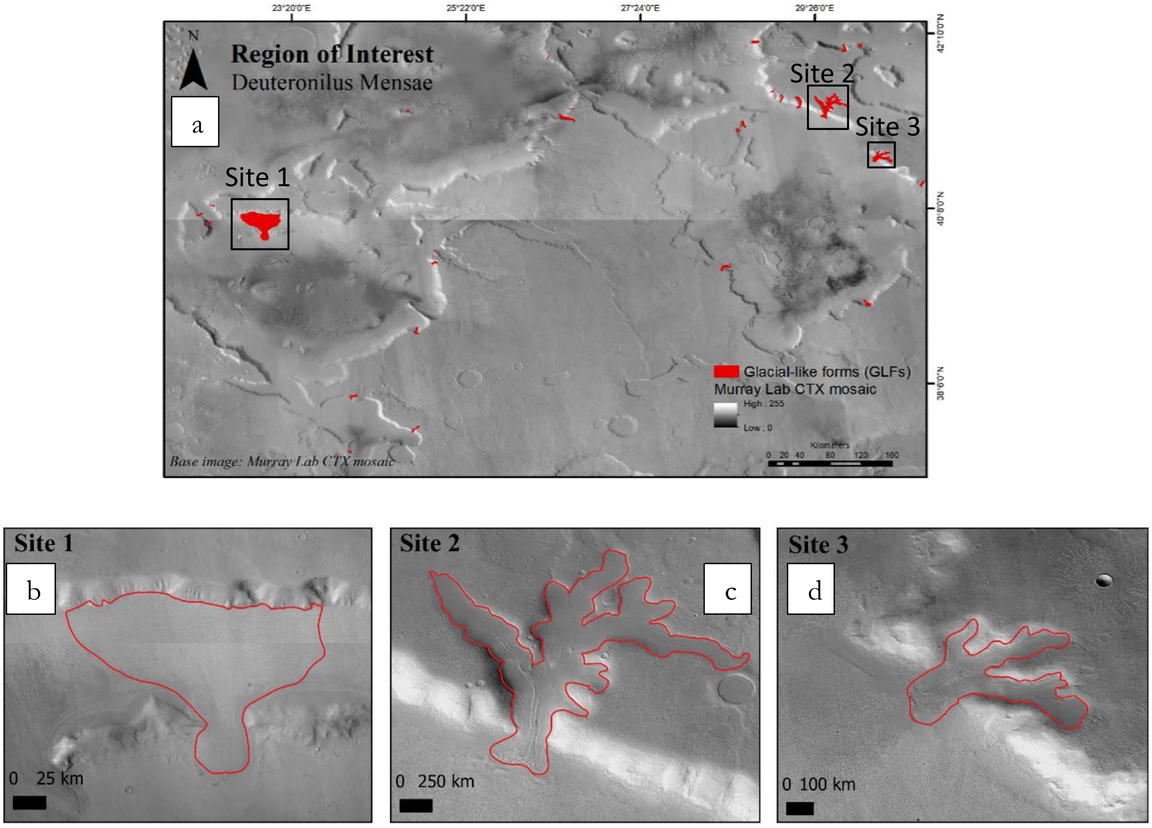

Figure 14: The selected sites marked in the map above. A close view of the three sites in small windows. Site 1 covering the largest area among the 23 GLFs followed by site 2 and then site 3.

Selected Radargram IDs for the three sites		
Site 1	**Site 2**	**Site 3**
S_03369902_RGRAM	S_00685201_RGRAM	S_00799902_RGRAM
S_03634301_RGRAM	S_00720801_RGRAM	S_02546401_RGRAM
S_03695602_RGRAM	S_02557602_RGRAM	S_03364601_RGRAM
S_03975201_RGRAM	S_04493401_RGRAM	S_03442401_RGRAM
S_04382001_RGRAM	S_04613402_RGRAM	S_04827001_RGRAM
	S_04862601_RGRAM	

Table 4 Radargram IDs. Listed in the table are SHARAD radargram IDs selected for each site.

4.2. Selected SHARAD radargrams and clutter simulations

This section explains radar observations covering the selected three sites and their processed outputs. SHARAD radargrams were selected based on their coverage of the three different sites. Since all the three GLFs cover a larger area, multiple radargrams from different orbits are chosen for each location.
In the following few subsections, the radargrams and the processed outputs of the radargrams for the selected sites are described.

4.2.1. Site 1

GLF-site 1: refer to figure 14b.

As reflections beneath the target landforms cannot be predicted by clutter simulations, these are useful for differentiating surface off-nadir echoes from subsurface ones. Therefore, a step using the CO-SHARPS clutter simulator was performed to build a comparison and highlight the subsurface echoes. In figures 15b and 15c, the radargram and its clutter simulation are shown, respectively, which covers site 1 along with SHARAD's track for this observation (figure 15a). From the radargram and its clutter simulation it is possible to differentiate subsurface echoes. Since the clutter simulation only shows surface returns and off-nadir surface clutter, they can be used to distinguish the subsurface interfaces from off-nadir surface clutter. Figure 15 could help build a comparison between the original and the processed radargram. The following points could assist in better understanding the figure:

- As shown in figure 15a, the yellow pointer is at the location of the GLF at site 1 marked in the Themis global mosaic. Subsequently, the location of the GLF in the radargram figure 15b can be seen at the yellow position bar.
- In figure 15b, arrows are employed to mark certain areas of interest where subsurface interfaces are visible. A closer inspection of figure 15 would show the subsurface echoes are marked by blue arrows in figure 15b; these echoes are visibly absent in figure 15c. It can be noticed that the blue arrows pointing at subsurface echoes (15b) are not consistent with the clutter simulation (15c). The blue arrows indicate a few specific locations where possible subsurface interfaces can be seen. Because the clutter simulations do not show any reflectors at depth; it provides strong indication of echoes visible in the radargrams to be candidates for subsurface echoes.
- The green and red arrows mark the surface reflections and clutter, respectively. Echoes that are observed in both; radargram (15b) and clutter simulation (15c) are marked as clutter in red arrows.
- In the clutter simulation, the thin yellow line following the surface trail of the radargram represents the MOLA surface topography.

At multiple locations in figure 15b, signals arising from the subsurface can be candidates for subsurface layers/interfaces. What is striking about figure 15b is that the subsurface echoes are commonly visible where a peak-echo strength is observed. As the data is in time delay (SHARAD's operational characteristics), it can be suspected that the peak -echo strength could be because of elevated landforms. As the signal from elevated landforms would appear earlier than its surroundings, the echoes in the radargrams appear as peaks. Interestingly subsurface echoes (marked by blue arrows in figure 15b) are visible consistently where the peaks or the slopes of the peaks are present in the radargram.

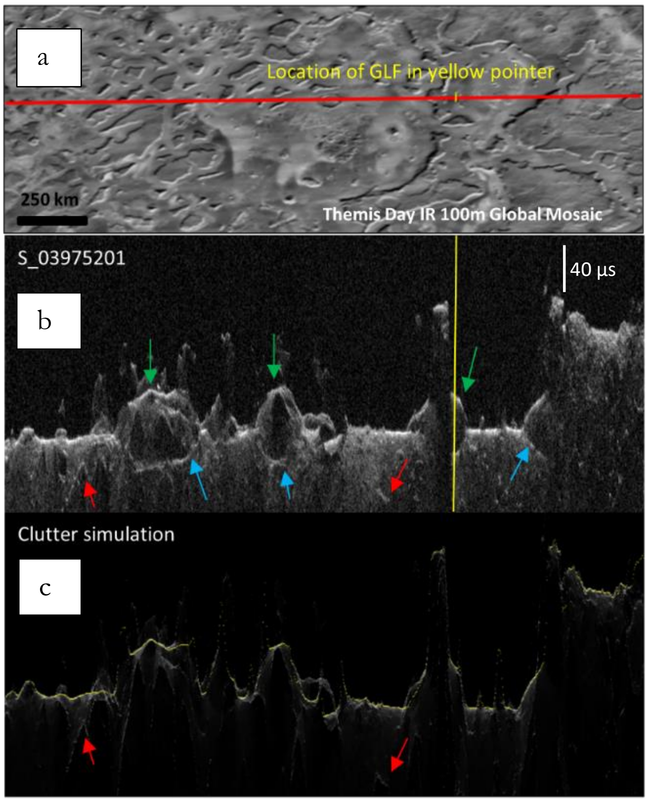

Figure 15: SHARAD track, original radargram and its clutter simulation. a) SHARAD track for the subsequent radargram. Yellow pointer shows location of the GLF. b) Original radargram-green and blue arrows show surface and subsurface reflections, respectively. Red arrows pointing at clutter. c) Clutter simulation with absence of subsurface echoes and visible clutter pointed at in red arrows.

Moving ahead, a zoomed-in view of the five SHARAD tracks selected for site 1 and their respective five radar images are compiled in figure 16. Figure 16 has five rows; each row comprises the SHARAD track, radar observation, and its clutter simulation. The Viking colorized global mosaic was utilized as background image for showing the SHARAD tracks to get a better view of the topography.

In figure 16 row 1, the track location of radargram id S_04634301 is shown along with its clutter simulation. The markings on track location like a-a' covers the extent of the GLF marked in the respective radargram. The white arrow in the radargram shows the extent of the GLF present in the radargram. Similarly, the observations of other 4 rows are marked for the location of the GLF. In the radar observations shown in figure 16 subsurface echoes are marked by blue arrows. These are marked based on their absence in the clutter simulations. Due to the absence of the subsurface reflections in clutter simulations of the radargrams, strong evidence of under the surface interfaces can be observed in site 1.

The nearby crossing of the GLF-site 1 by the five tracks displayed in figure 16 shows overall consistency of subsurface echoes across the different sections of the GLF while exhibiting slightly varying details of the subsurface.

The inspection of the radargrams can be summarized in the following points and would be useful to analyze the radargrams for site 2 and 3 as well:

- Surface detections arising from the surface of the GLFs and around the GLFs are marked by green arrows (figure 15b). The MOLA topography's yellow trail helps mark the signals from the surface.
- Subsurface detection: Those radar reflections which are not present in clutter simulations.

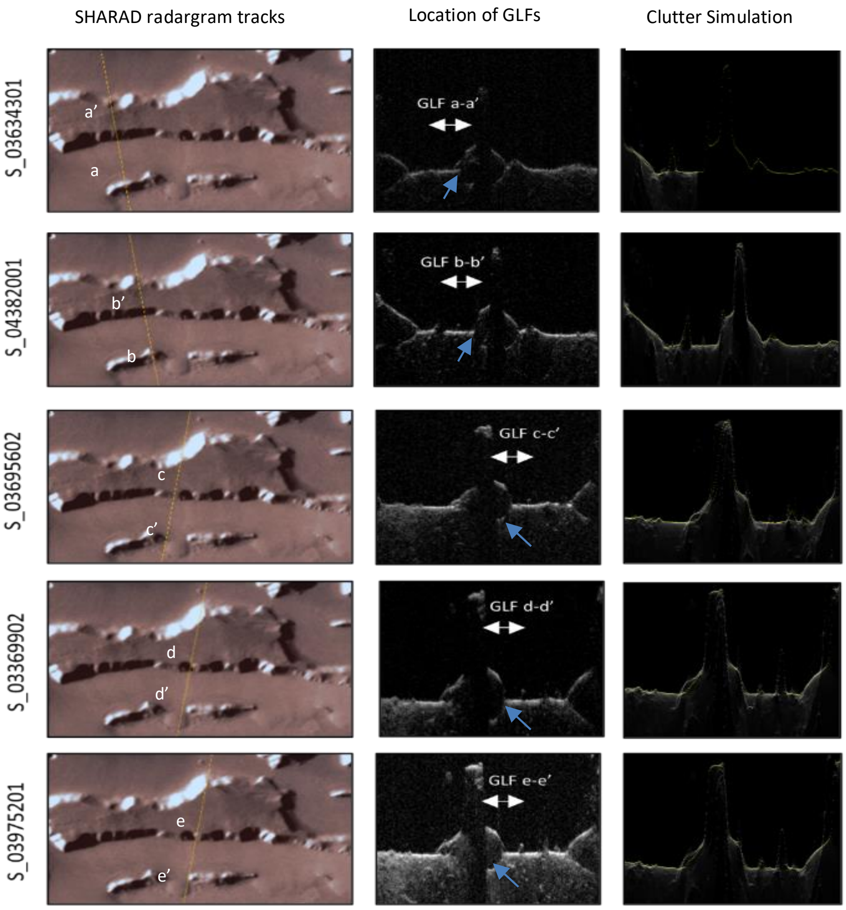

Figure 16: Chosen radargrams tracks for site 1 in the first column. A close up of the radargram where the GLF is located in site 1 is in column 2 and its respective clutter simulations in column 3. The markings on the track like a-a' shows the direction in which the instrument captured the radar signals, also marked in the radargram. Tracks shown on background image: Viking Colorized Global Mosaic.The contrast and brightness of the radargrams in figures 15 and 16 were adjusted using the GNU manipulation program.

4.2.2. Site 2

GLF-site 2: refer to figure 14c.

In this section, the results from site 2 are explained. Figure 17 provides the results acquired after analyzing the radargrams and their clutter simulations. The markings and the representation of the results are in the same format described for site 1 in sub-section 4.2.1.

Interestingly in the radargram-figure 17b, subsurface echoes marked by blue arrows are visible in areas slightly away from the GLFs. Consistently appearing under the peaks, these signals are not observed in clutter simulations and are thus plausible candidates for the subsurface interface. There was no evidence of echoes occurring from beneath the GLF-site 2, however, there was a resemblance between the results from site 1 and site 2. Similar to results from site 1(figure 15), in site 2, echoes are visible in areas apart from the GLF (figure 17b). However, the observed location of the GLF (yellow pointer) in figure 17a, 17b shows no evidence of subsurface echoes. When zoomed at the GLF-site 2 shown in figures 17d, 17e, there is no evidence of under the surface echoes seen as the yellow pointer bar moves over the GLF.

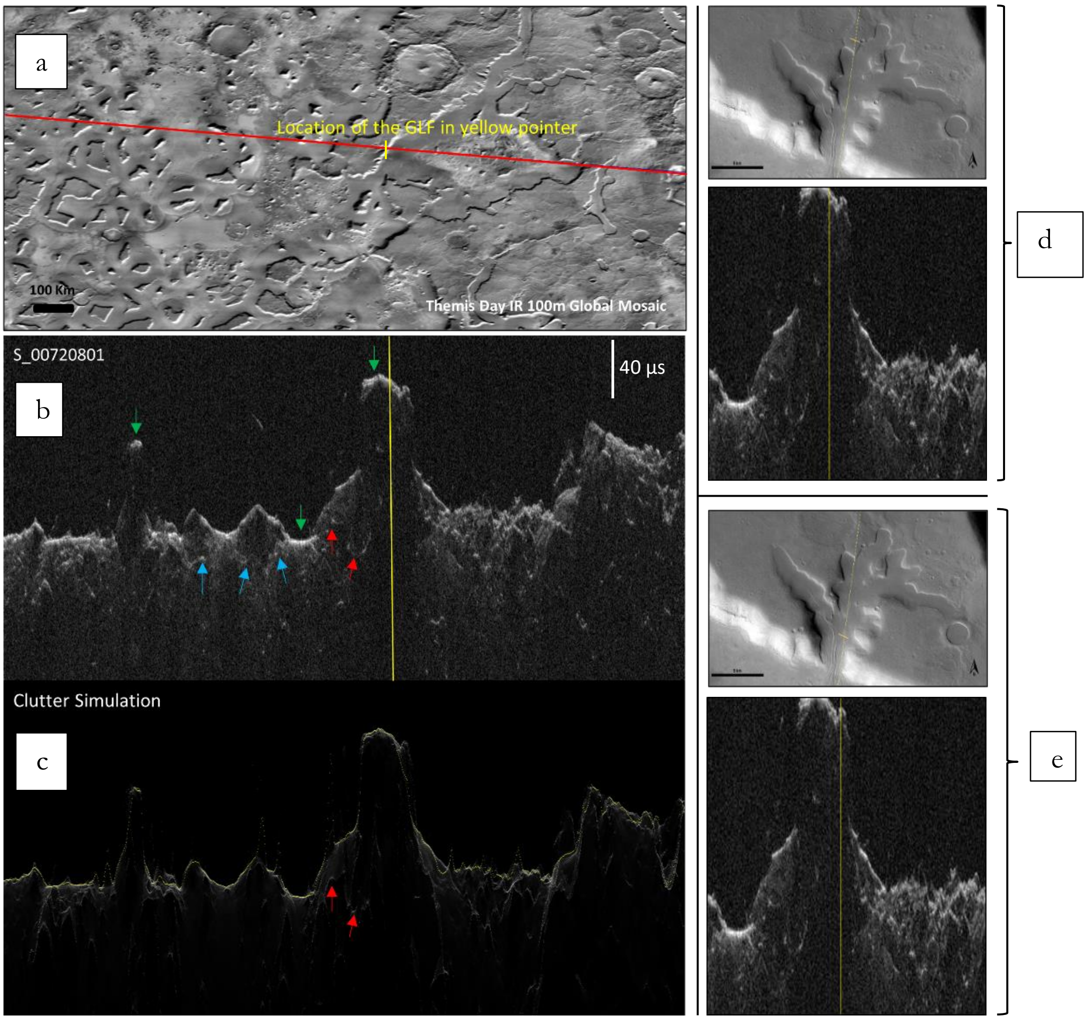

Figure 17: SHARAD track, original radargram and its clutter simulation. a) SHARAD track for the subsequent radargram. Yellow pointer shows location of the GLF. b) Original radargram-green and blue arrows show surface and subsurface reflections, respectively. Red arrows pointing at clutter. c) Clutter simulation with absence of subsurface echoes and visible clutter pointed at by red arrows. d) On the right, yellow pointer at the area slightly above the GLF in the gray imagery. Zoomed-in view of the radargram where the yellow position bar is present exactly where the pointer is shown in the gray image. e) The bottom window shows yellow pointer crossing the GLF in the gray imagery. The yellow position bar in the radargram moved as the pointer crosses through the GLF. Zoom in to look at the pointer in d) and e).

4.2.3. Site 3

GLF-site 3: refer to figure 14d.
In this section, results from site 3 are explained. This is the smallest site among the three chosen for this study, with an area of 39.5 km^2. In figure 18b, at the location of the GLF, there are no reflections visible that can be labeled as subsurface echoes. Moreover, the radargram is rather noisy, probably due to off-nadir reflections from the surrounding chaotic terrain of Deuteronilus Mensae, which was observed using MOLA surface topography. At specific locations in the radargram (18b) marked by blue arrows, faint subsurface echoes can be seen; however, it is difficult to conclude with confidence that these are subsurface echoes because of the noisy nature of the data and more prevalent off-nadir clutter.

Moreover, echoes from any subsurface interface are slightly stronger than the clutter at the same time delay associated with the surface reflection (Seu et al., 2007). Interfaces observed at a greater time delay could also possibly indicate the presence of subsurface echoes and help detect under the surface interfaces.
Overall, the result from site 3 shows no evidence of subsurface echoes at the location of the GLF. But in other areas where the track passes through, visible echoes could be coming from the depths. The next chapter will discuss the possibility of other locations bearing subsurface echoes.

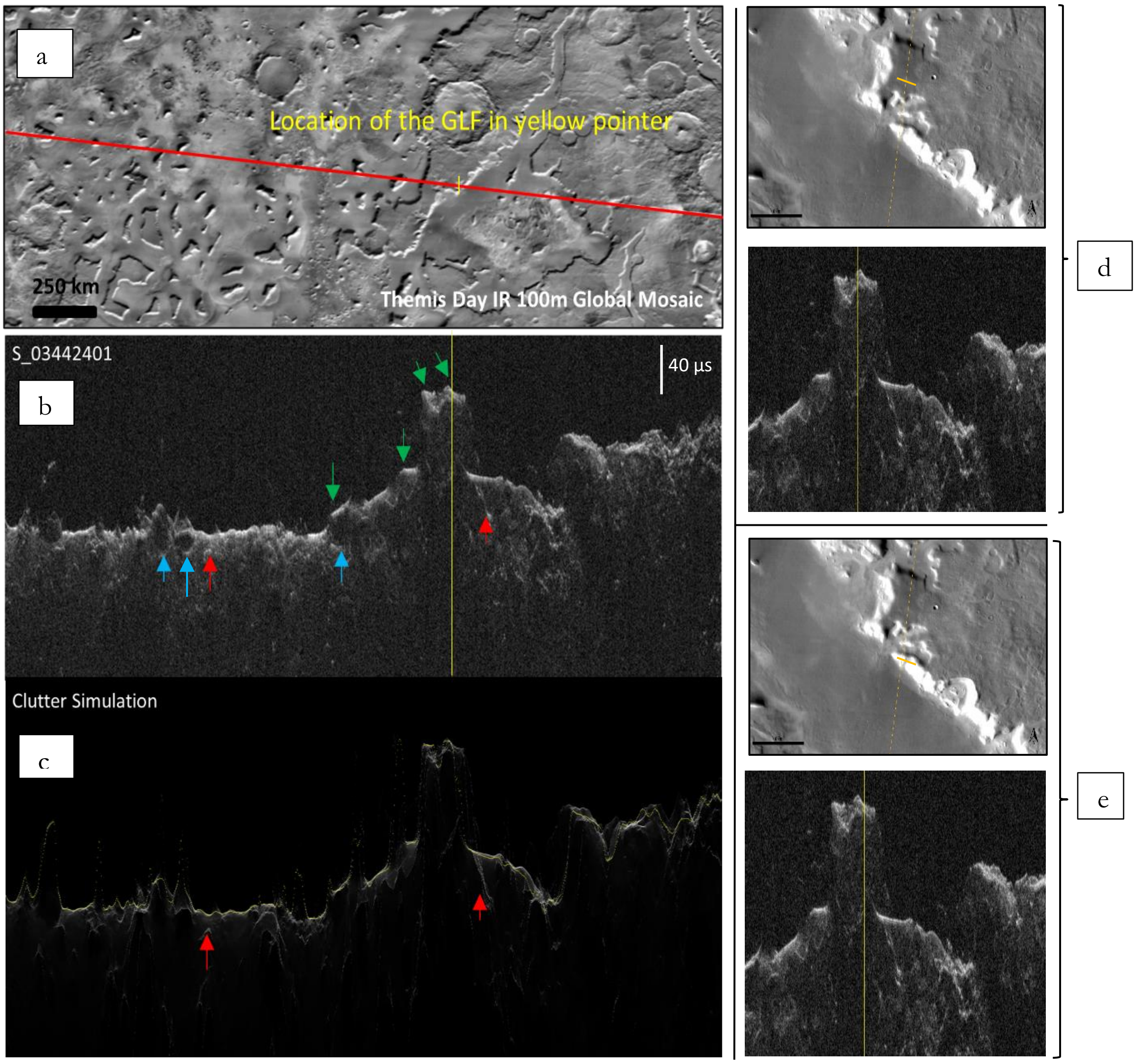

Figure 18: SHARAD track, original radargram and its clutter simulation. a) SHARAD track for the subsequent radargram. Yellow pointer shows location of the GLF. b) Original radargram-green and blue arrows show surface and subsurface reflections, respectively. Red arrows pointing at clutter. c) Clutter simulation with absence of subsurface echoes and visible clutter pointed at in red arrows. d) On the right, yellow pointer at the area slightly above the GLF in the gray imagery. Zoomed-in view of the radargram where the yellow position bar is present exactly where the pointer is shown in the gray image. e) The bottom window shows yellow pointer crossing the GLF in the gray imagery. The yellow position bar in the radargram moved as the pointer crosses through the GLF.

Interestingly, apart from the results from the region of interest (GLF sites), there are other areas shown in Figures 15b, 17b, and 18b by blue arrows, where subsurface echoes are visible. Taken together, these results from all three sites suggest that there could be interesting locations or landforms bearing subsurface interfaces. Therefore, the next chapter moves on to discuss more about these observations and infer what I best understand from them.

5. DISCUSSION

5.1. Suitable target landforms

The first question in this study sought to determine suitable target GLFs for exploring subsurface layers. As explained in chapters 3 and 4 in detail, CRISM summary products were utilized to find suitable target GLFs in the study area based on evidence of hydrous minerals. I found no significant traces of hydrous minerals, phyllosilicates, or hydrated silicas. This finding also partially supports the work of Pan and Ehlmann (2018), where Deuteronilus Mensae was studied extensively for hydrous minerals. Though Pan and Ehlmann suggested that Fe and Mg phyllosilicates can be found in the marked area (close to site 1) in figure 19b (blue star symbol), on the other hand, I notice that the levels of phyllosilicates investigated at the location using CRISM summary products in figure 19c are faint and negligible. In figure 19c, I observe a slight indication of mineral deposits where the ridge-like feature is located. However, it cannot be concluded with confidence that there are Fe and Mg phyllosilicates deposits.

Apart from the contradictory observation about the Fe and Mg phyllosilicates, there was one similarity observed in the study region (figure 19b blue box) from Pan and Ehlmann's map. Notice that in the blue box marked in figure 19b, no evidence of hydrated minerals is shown. Overall, the lack of hydrous and silica deposits in the studied region (figure 19 b blue box) aligns the findings of this study with those of Pan and Ehlmann.

Contrary to the expectations, no suitable targets were found based on CRISM summary products, leading to the selection of GLFs only based on their size and area covered. Therefore, the three larger sites more suitable for SHARAD's radargram resolution were chosen for this study and monitored for subsurface echoes.

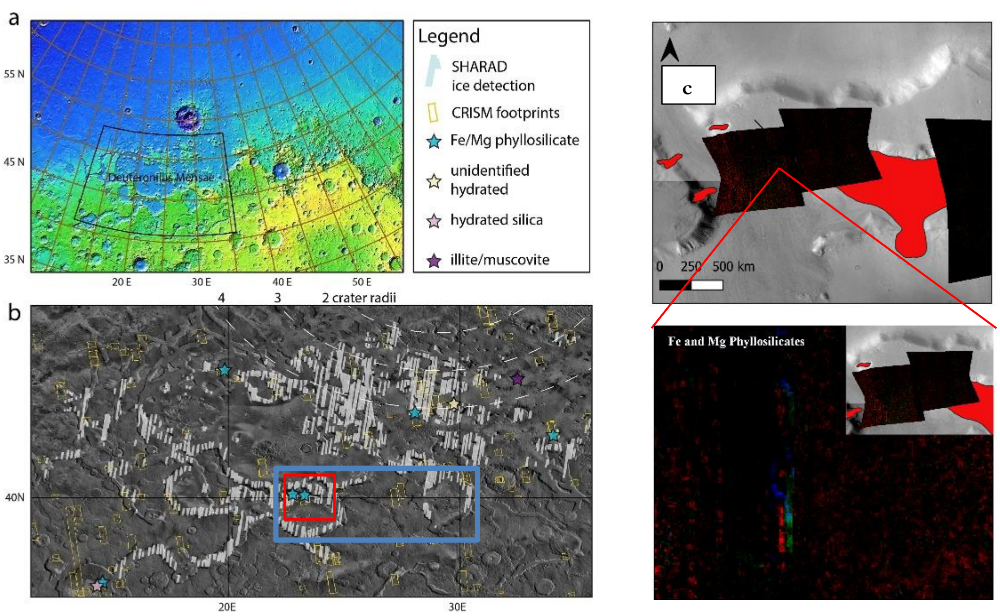

Figure 19: a) and b) Map showing mineral distribution taken from Pan and Ehlmann's study, as per their study Fe and Mg phyllosilicates are identified in the CRISM product FRT00013F15_07_BRPFMJ_MTR3. Red outline at the deposition of phyllosilicates also where site 1 is located. Blue box shows study area boundary and red box is the location of site 1. c) Observation from this study: The CRISM product is located near site 1 monitored in this studied. As illustrated faint colours are visible however I believe they are not significant enough to be identified as phyllosilicates deposits.

5.2. Techniques to investigate echoes

This study set out with the aim of employing detection techniques to identify subsurface echoes. However, it is critical first to reveal and study 'what' can be referred to as subsurface interfaces. Clutter simulator is an effective tool for understanding what can be called subsurface interfaces. Thus, it was essential to study the simulations thoroughly as part of the aim of this study. Before moving ahead with any form of detection technique of subsurface echoes, clarity of the target areas and features of these subsurface interfaces is vital, which is essentially what this study aimed to do. The CO-SHARPS clutter simulator is an excellent tool to distinguish under the surface echoes from noise or unwanted clutter; an example image is shown in figure 20. Figure 20 displays the radargram S_02780502 and its clutter simulation and helps distinguish clutter in red arrows from possible subsurface echoes in blue arrows marked in figure 20a.

Evidently, one can go ahead with automated detection techniques to classify or identify layers. Still, even in that case, I believe investigating subsurface echoes using the simulator is an inevitable step. It allowed dealing with a major issue of off-nadir reflections and experimenting with the adjustable parameters, an essential step before moving ahead with advanced processing and detection.

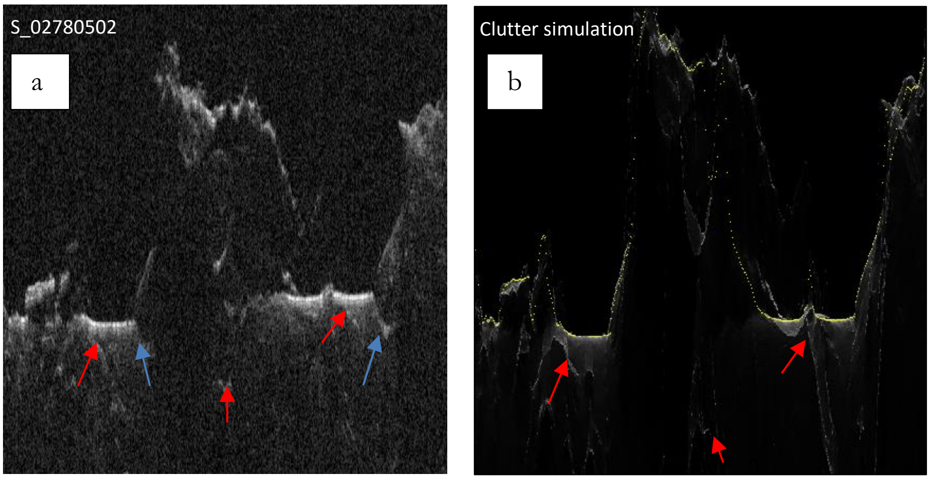

Figure 20: a) Radargram ID S_02780502 with blue and yellow arrows pointing out subsurface echoes and clutter respectively b) clutter simulation with absence of subsurface echoes and clutter marked in red arrows.

5.3. Subsurface echoes under target areas

One of the objectives of this study was to see which target landforms bear under the surface layers. In the three GLF sites investigated, either thin deposits are present near the base of the GLF, or there are no subsurface echoes. Although in one of the sites I observed faint echoes arising from under the surface of the GLF, contrary to expectations, the visible interfaces are not evident in all the three targeted sites. A possible explanation for these results may be the relatively small size of the GLFs. There are contributions to the SHARAD signal from features smaller than MOLA DEMs resolution of ~463 m. However, identifying such small features or layers would only be possible if higher resolution DEM were available for the clutter simulator. Since CO-SHARPS only uses MOLA DEM of the above-mentioned resolution, there are limitations to fully explore the subsurface of GLFs.

Additionally, factors like surface roughness also play a major role in the echo strength of any given site. Echo strength tends to decline with increasing roughness (Campbell et al., 2013) and, therefore could limit the signals received from the target areas. SHARAD roughness parameters and MOLA-derived roughness are thoroughly studied by Campbell (2013) for several regions on Mars, such as Elysium and Amazonis Planitia. Analyzing surface roughness and its implications is beyond the scope of this study and could be an initial step to start from for future work.

5.3.1. Patterns in the subsurface echoes

In the radargrams explained in chapter 4 for the three sites (figure 15, 17 and 18), a distinctive pattern in the subsurface echoes from and around the GLFs can be noticed. Figure 21 (below) shows an example of the subsurface echo disintegrating from the surface level and forming another interface. Another study of lobate debris aprons (LDAs) in the mid-northern latitudes of Mars shows a similar pattern. Figure 21a is taken from the study by Jeffrey J Plaut (2009), which shows the split in the subsurface echoes in the lobate debris aprons of the Deuteronilus Mensae region. This pattern is similar to what research has observed in the polar layered deposits (Picardi et al., 2005) and Hellas basin (Holt et al., 2008) of Mars. Besides the split of the interface, in figures 21b and 21c it can be noticed that the subsurface echoes appear tilted or diagonal (blue arrows), which is different from what one expects from underground layers studied in the polar region of Mars. However, such an appearance would be because the data is in time domain. If the time delay data is converted to depth-corrected radargram by inputting a di-electric constant suitable for the area, the diagonal appearing echoes would be more levelled. Figure 22 shows the radargram S_03975201 and its depth-corrected images using di-electric constant value of 3.15. Notice the tilt in the echoes are not visible in the depth-corrected image in figure 22.

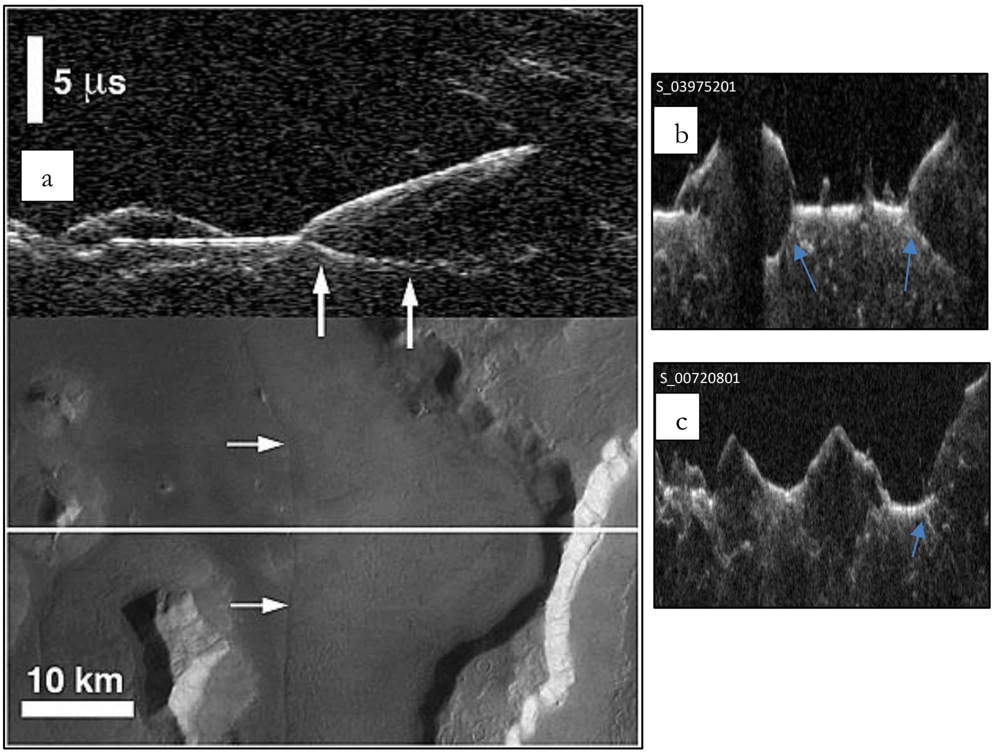

Figure 21: a) Radargram showing subsurface echoes splitting from the base of the surface of an LDA, marked in white arrows in the radargram and in the grayscale image. Image taken from Jeffrey J Plaut (2009) study. b) and c) Similar to the study by Plaut, pattern visible in the subsurface echoes in the chosen radargram for this study.

Figure 22 is an example image to understand the possible reasons behind the appearances of the subsurface echoes. With a suitable di-electric constant, depth correction can be performed easily using CO-SHARPS boutique, however, it is an optional process. Since depth correction leads to under-sampling, data loss can be expected. Therefore, this study has relied on time-domain radargrams to look for subsurface echoes.

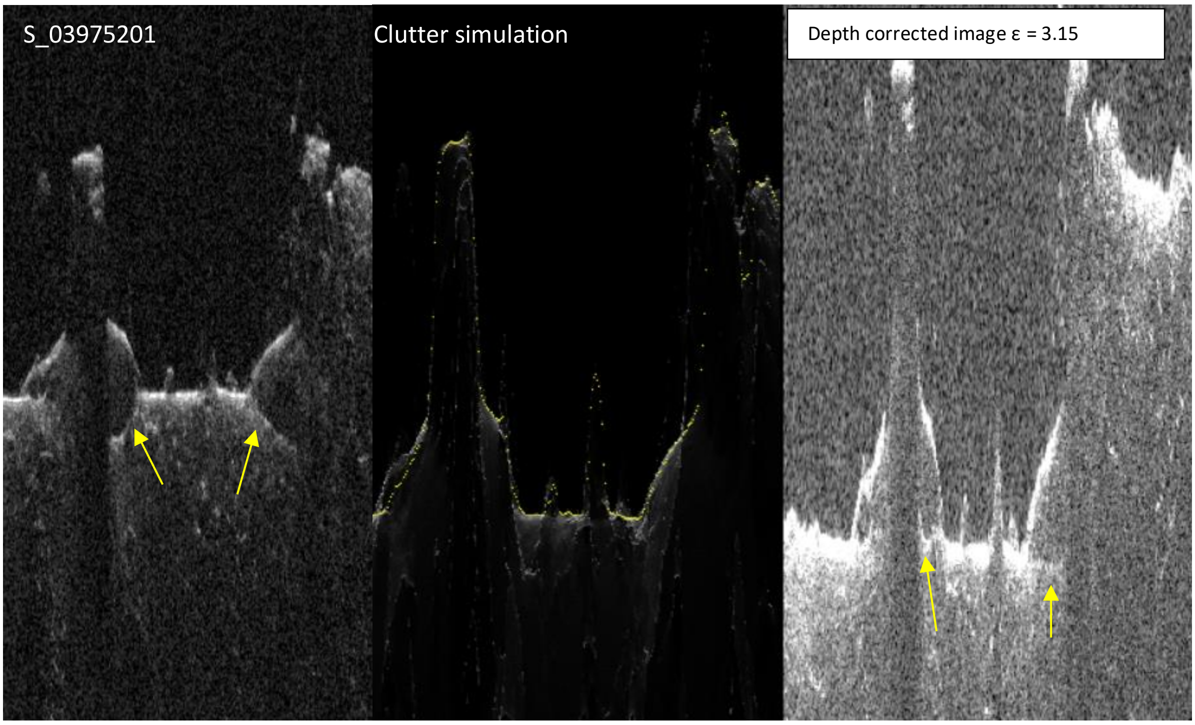

Figure 22: Original radargram and its depth-corrected image using di-electric constant value of 3.15. The tilted appearance of the subsurface echoes seem more levelled in the depth-corrected image.

Moving ahead, in order to further judge whether the visible echoes can be categorized as subsurface echoes; depth plots maybe be a helpful tool.

Depth plots graphs the pixel depth and raw pixel value of the radargram in Y and X axis respectively. These plots can be generated using the JMARS software (also described in section 3.2). Subsurface echoes show higher intensity than sidelobes or clutter (Seu et al., 2007, 2004), and this trait can be used to distinguish the echoes from noise. A higher intensity indicates a higher pixel value; therefore, depth plots could help locate the subsurface echoes. In figures 23a and 23b radargrams with yellow vertical position bars are shown. The plots adjacent to them graph the position bar and generates a depth plot. The depth plots shown in figure 23 show peaks representing signals probably from the surface and the subsurface interface. Notice that these peaks are more significant in pixel values than the pixel values of noise. Notice the two peaks in both the depth plots. The first peak most likely is due to the higher power achieved from the surface interface (higher pixel values), and the second peak arises at the location where subsurface echoes are visible. The fade-in power is expected from the subsurface interfaces, and the second lower peak is strong evidence of that. The second peak is also visible at a greater time delay in both figures 23a and 23b, which hints at possible interfaces lying under the surface.

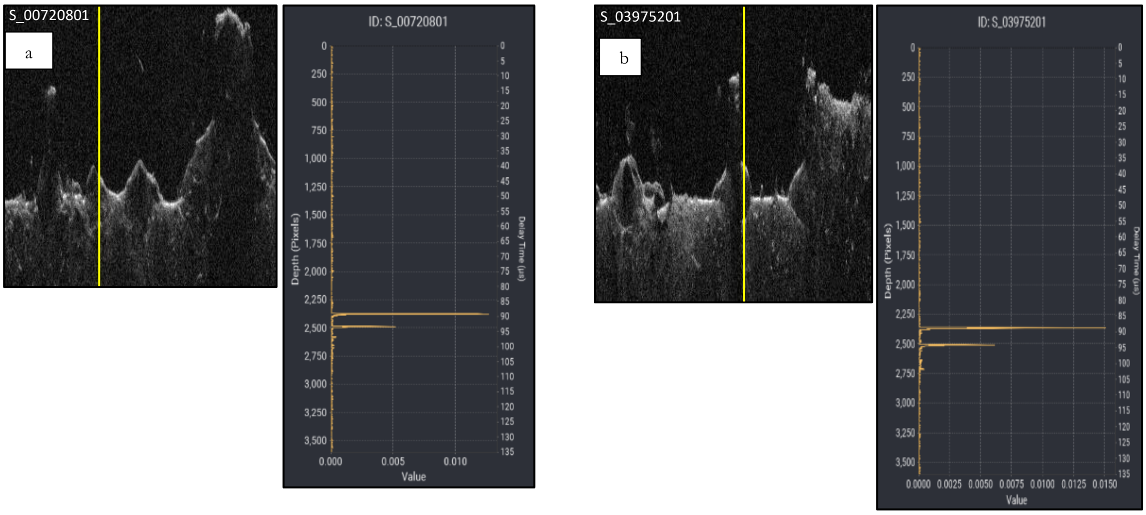

Figure 23: Depth plots shown adjacent to two different radargrams in a and b. The depth plots show the reading of the radargram where the yellow line is present.

5.4. Landforms bearing subsurface deposits

As interpreted earlier in chapter 4, subsurface echoes are visible in radargrams at multiple locations apart from the GLFs. Consistently, the location of the subsurface echoes is where a peak echo-strength is evident, as shown in figure 24. The orange arrows indicate the peak-echo strength, and the blue arrows show subsurface echoes. When looked closely using other datasets, these appear to be raised, peak-like features that differ from the location of GLFs. It can be argued that those subsurface echoes are generated due to double bounces or could be surface clutter which are common problems with radar datasets. However, three major points support the hypothesis of the echoes being a subsurface interface; 1) comparison of radargrams with clutter simulations and absence of subsurface echoes in the simulations 2) the common pattern seen in subsurface echoes, and 3) other topographically interesting features bearing the subsurface deposits which are directly or indirectly associated with glaciation. The study region Deuteronilus Mensae, located in the northern mid-latitudes is the most topographically dramatic region of the dichotomy boundary with a history of glaciation (Jeffrey J Plaut et al., 2009). Since the terrain of this area is comprised of several features showing evidence of glacial land systems, channels, and valleys (Head et al., 2006), it is reasonable to consider them as potential features for bearing subsurface layers. These results are therefore, in agreement with previous studies on mid-latitudes where mesas, remnants of the regional ice sheet (Baker and Head, 2015), and valleys are considered to be strongly associated with the glacial land system on Mars (Head et al., 2003; Nazari-Sharabian et al., 2020).

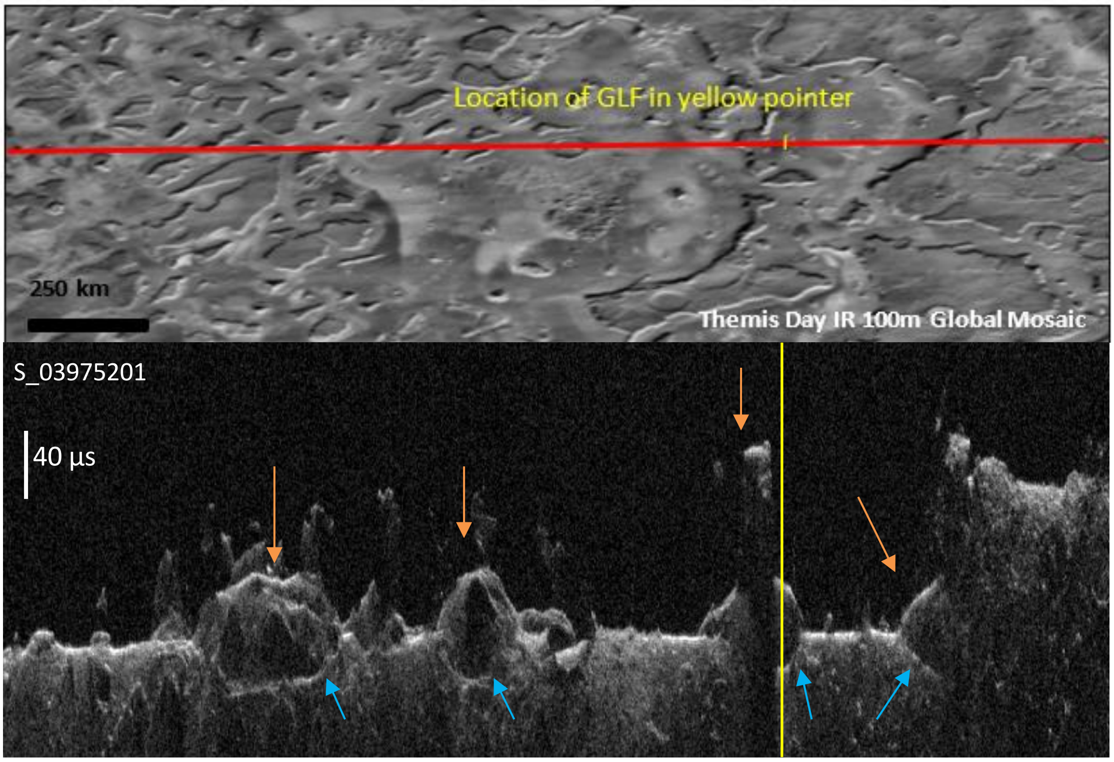

Figure 24: Orange arrows pointing out peak-echo strengths. Subsurface echoes marked in blue are consistently seen where the peaks are visible. Orange arrows pointing out peak-echo strengths. Subsurface echoes marked in blue are consistently seen where the peaks are visible.

The raised peak-echo strength shown in the radargrams in figure 24 arises from what most studies call remnants and mesas. This indicates that there might be other landforms bearing subsurface echoes.

In order to get a better view of the possible sources of these peak-echo strengths, a geological map of Deuteronilus Mensae was referred to and is shown below in figure 25a.

As illustrated in figure 25a, the north of Deuteronilus Mensae was mapped by Lennard Pauw (2022), his work in progress study aimed to elucidate the appearances and morphology of this region. The map is of interest for this study due to its coverage of the Mensae region around GLF-site 1(figure 14b, ROI for this research). Since the map covers a small area (GLF-site 1 and nearby region) of interest for this study, I intend to see the morphology and elucidated features in the area, which could have led to peak-echo strengths in the radargrams. The motive for referring to the map was to better understand the potential origins of these peak-echo strengths. The following points describe figure 25 in detail.

- Figure 25(b,c) shows that the orbit track 33699 passes through the small, raised landforms called remnants described in the legend and pointed out on the map. This track also crosses valley walls and thick plain materials, of which the echoes marked by blue arrows are visible in the radargram S_03369902.
- White boxes in figure 25b show the extent of the radargram windows shown in 25d and 25e
- Figure 25b shows the above-mentioned track over the Viking global mosaic with GLF-site 1 pointed out.
- Figure 25c shows a small section of the geological map where GLF-site 1 is marked.
- Figure 25b shows that the track passes through remnants and valley walls; this can be understood by referring to figure 25c, where the geology of the region is illustrated along with its legend at the bottom.

- Figure 25d shows a small section of the same radargram S_03369902 in which a peak-echo strength is visible when the track passes through the remnants. Similarly, in figure 25e the peak-echo strength is visible where the track passes through the valley walls shown in the white box in figure 25b.

Likewise for GLF-site 2 and 3, it can be observed in Figures 26a and 27b that plateau material and upper plains, as described in (Baker and Head, 2015), have the potential to bear subsurface deposits. In figure 26a, orbit track 7208 passes through plateau material and upper plains; figure 26b shows the peak-echo strength arising from these features, also marked in the white box in figure 26a.
In figure 27(a,b), since the orbit track 34424 lies closer to track 7208, the area and the feature covered by the tracks are similar, and so are some of the geological observations as seen in the Viking mosaic.
Altogether the results from all three sites depict subsurface echoes in areas other than GLFs; these areas, when looked at closely using Viking colored mosaic and context camera imagery, show the occurrence of valley walls (Pauw et al., 2022) and plateau material (Baker and Head, 2015).
As stated before, research believes that an ocean existed on Mars several hundred billion years ago and a lower shoreline of the ocean is where Deuteronilus Mensae is located. The origin of subsurface layers from the valley walls, remnants, or what most studies call mesas, is interesting because of the possible origins of these landforms. Many landforms in the region are protected remains against deep water erosion (Nazari-Sharabian et al., 2020) and thus could be the source of subsurface layers. In the study region, since glacier-like forms, valleys, and plateau material lie in the proximity of 150-300 km to each other, it is possible that they originated under similar dramatic climatic changes and glaciation processes. Lobate debris aprons (LDAs), which are prevalent in this region, are also a significant part of the glacial land system on Mars and are often found close to the GLFs. Since LDAs are known for bearing volumes of subsurface ice, it is likely that the interesting features like mesas around ice-bearing LDAs could also show evidence of subsurface deposits or ice due to the large-scale movement of polar ice to the mid-latitudes during the mid-latitude glaciation period which ended about two million years ago.

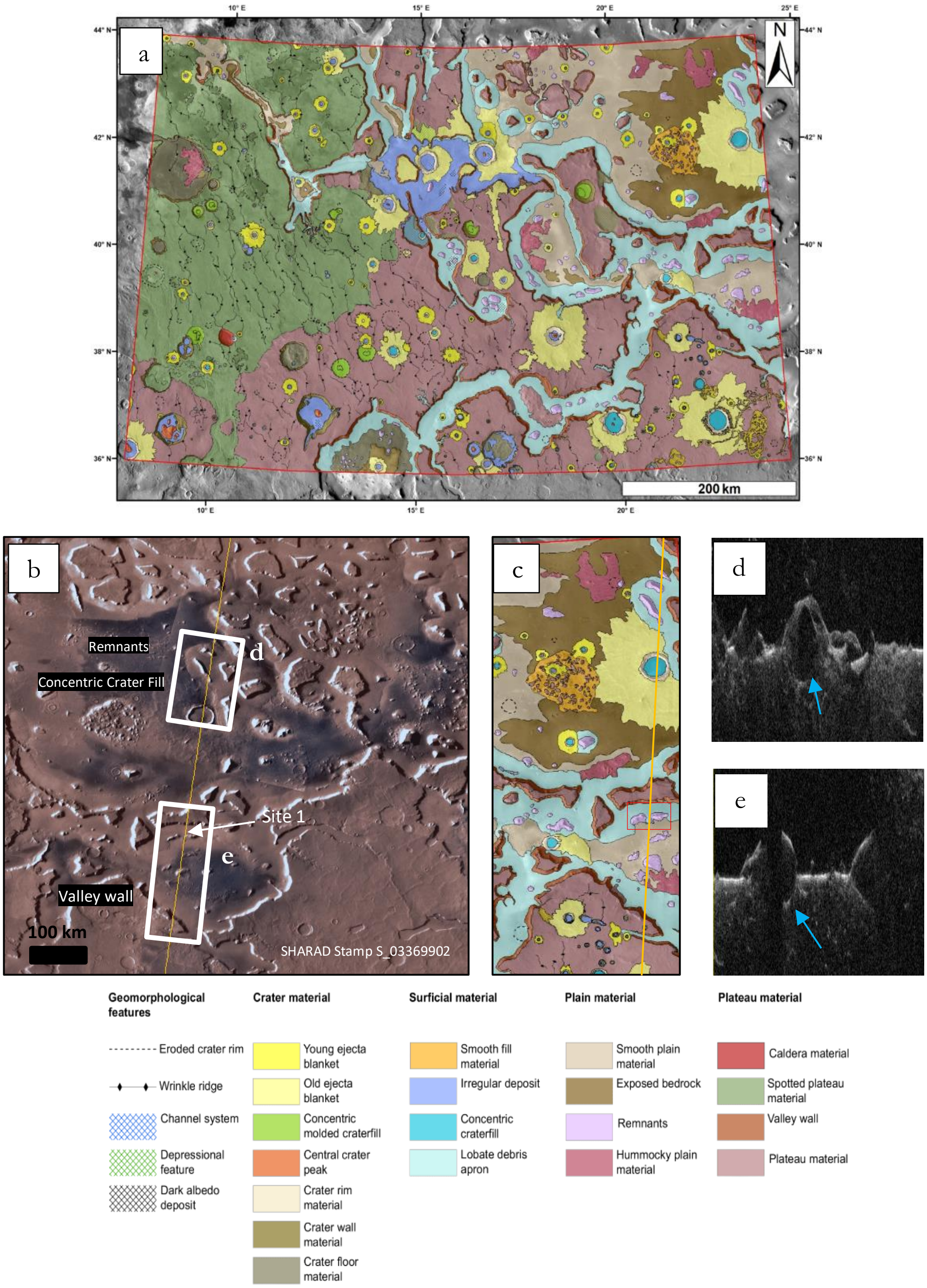

Figure 25: Map taken from Lennard Pauw's geological study in the north of Deuteronilus Mensae. A small section of the map shown in c) is of interest for this study. b) SHARAD orbit 33699 passes through site 1 shown in orange line. The white boxes mark the area covered by radargrams displayed in d and e. c) Small section taken from the map which illustrates the area where site 1 is present (red box). d) Shows the cross-section of the area marked in the white box in b, under the peak echo strength. Layers are visible where the track passes through remnants. e) Shows the cross-section of the area marked in the white box in b, under the peak echo strength layers are visible where the track passes through valley walls.

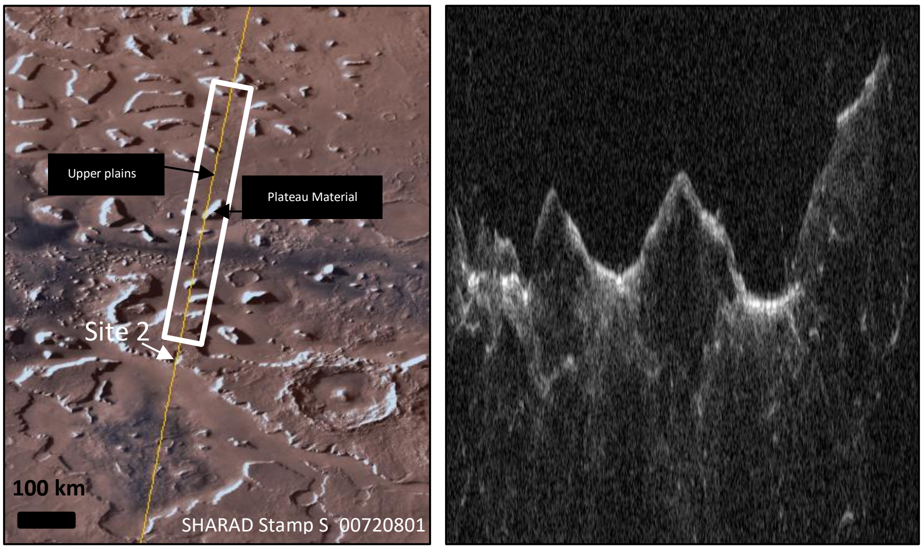

Figure 26: Track covering site 2. The coverage of the white box shows the extent of the radargram on right. Peaks visible in the radargram where plateau material is present. Subsurface echoes can be observed in the radargram. Refer figure 17 for overview of the radargram and clutter simulation.

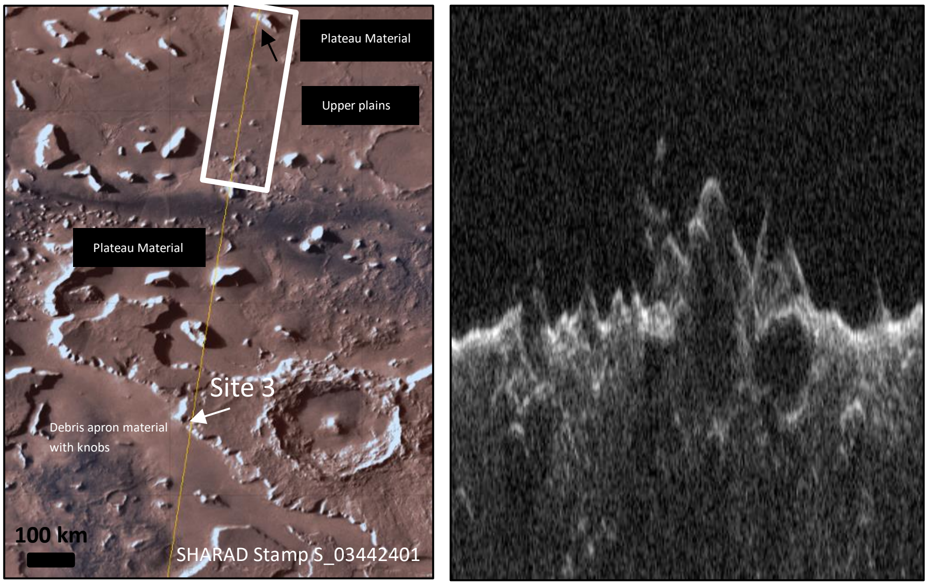

Figure 27: Track covering site 3. The coverage of the white box shows the extent of the radargram on right. Peaks visible in the radargram where plateau material is present. Subsurface echoes can be observed in the radargram. Refer figure 18 for overview of the radargram and clutter simulation.

6. CONCLUSIONS AND RECOMMENDATIONS

This study aimed to analyze the subsurface of GLFs using SHARAD radargrams to acquire an overview of the prevalent absence or presence of subsurface deposits. With the help of CRISM summary products and clutter simulations, an attempt was made to investigate the debris-covered glacier-like forms. The methods chosen to carry out this study involved examining CRISM summary products for evidence of hydrated minerals; no clear evidence of mineral deposits was visible in the study area. It was only in a few sites where summary products overlapping with the GLFs were found. To see the surface composition of the GLFs, rather than examining the CRISM images in-depth and building a mineral map, this study relied on looking at the overlapping summary products of specific minerals. To build a mineral map of the area, more CRISM images should be examined and processed from scratch.

The methodology continued with generating clutter simulations of the radargrams for the target sites and comparing them with the original radargram. I observed subsurface echoes in the target sites selected. However, they are not significant enough to be concluded as subsurface deposits or layers. One of the more important findings from this study was the presence of subsurface echoes in other features (non-target sites) apart from LDAs and GLFs. Time delay plots and clutter simulations provided strong evidence of subsurface echoes visible in locations other than GLFs in the chosen radargrams. I believe when stating the suitability of the GLFs for evidence of water, it is integral to look at the radar datasets. Radar evidence and prediction signals from clutter simulations build a strong base to understand what can be called as subsurface echoes and further comment on the possibility of the presence or absence of subsurface layers. This study led to the observation of echoes arising from the subsurface of GLF-site 1 and echoes arising from other features like valley walls and plateau material as well. The presence of subsurface echoes makes a GLF suitable for further studies. It should also be noted that it is challenging to explore the subsurface of the extremely small GLFs due to the resolution of the radar data.

Since this study extensively used CO-SHARPS clutter simulator, it should be mentioned that the SHARAD signal receives contributions from features smaller than MOLA DEM's resolution of ~463m. However, recognizing such tiny features or layers might be achievable only if the clutter simulator had access to a higher resolution DEM. Because CO-SHARPS only employs MOLA DEM of the aforementioned resolution, it is limited in its ability to properly investigate the subsurface of GLFs. The insights gained from comparing clutter simulations and radargrams may assist in later performing advanced detection procedures with the aid of automated techniques. Due to time constraints, this study was limited to assessing the presence or absence of subsurface echoes based on spectral indications and clutter simulations. Furthermore, it was anticipated that there would be challenges when dealing with a planetary dataset like SHARAD since so many factors affect a complex instrument like SHARAD, followed by heavy pre-processing of the raw data. It should be noted that the dataset must be handled and examined carefully for any subsurface echoes.

Although the current study is based on a small sample of selected sites, the finding suggests that the smallest of landforms like GLFs could help bridge the gap in our understanding of the glacial history of the topographically dense region of Deuteronilus Mensae. Additionally, radar evidence and prediction signals from clutter simulations provide a solid foundation for understanding what are known as subsurface echoes and commenting on the existence or absence of subsurface layers. To conclude, the findings from this study will be of interest to those studying the Martian glacial land system and trying to build a link between the viscous flow features and other landforms like valleys and plains in the northern mid-latitudes.

6.1. Recommendations

- A natural progression of the work would be to know what these subsurface echoes are. Taking into account the texture, di-electric properties, and other statistical parameters in the radargrams, more about the subsurface echoes can be discovered. To fully utilize the potential of the radargrams, edge-detection filtering and inversion techniques can be employed.
- An extension of the work done in this study could be focused on ice deposits in the GLFs. The composition of the detected subsurface echoes can be studied to further comment on the availability of ice layers.
- Apart from SHARAD, another radar dataset, The Mars Advanced Radar for Subsurface and Ionospheric Sounding (MARSIS) on Mars Express, can be employed to further explore viscous-flow features on Mars. With the upcoming updates and software development (PSI, 2020) customized to MARSIS data, research can be carried out more effectively.
- More broadly, research is also needed to look at the other areas of interest pointed out in this study, like valley walls and upper plains, to further build an understanding of the region both in terms of subsurface interfaces and geomorphologically. Probably with more research, areas of dense subsurface interfaces can be found in the mid-latitudes for this Deuteronilus Mensae would be a fruitful area for further work.

LIST OF REFERENCES

Adler, J.B., Anwar, S., Dickenshied, S., Carter, S., 2016. Sharad Radargram Analysis Tool Development in Jmars. Sixth Mars Polar Sci. Conf. 1–2.

Baker, D.M.H., Head, J.W., 2015. Extensive Middle Amazonian mantling of debris aprons and plains in Deuteronilus Mensae, Mars: Implications for the record of mid-latitude glaciation. Icarus 260, 269–288. https://doi.org/10.1016/J.ICARUS.2015.06.036

Bramson, A.M., Andres, C., Bapst, J., Becerra, P., Courville, S.W., Dundas, C.M., Hibbard, S.M., Holt, J.W., Karunatillake, S., Khuller, A., Mellon, M.T., Morgan, G.A., Obbard, R.W., Perry, M.R., Petersen, E.I., Putzig, N.E., Sizemore, H.G., Smith, I.B., Stillman, D.E., Wooster, P., Nerozzi, S., Diniega, S., JPL Jeffrey Plaut, N., Jpl, N., Charity Phillips-Lander, C., Cynthia Dinwiddie, S., Johnsson, A., Mischna, M., Adrian Brown, C.J., Research, P., Noora Alsaeed, L., Boulder, C., Rachael Hoover, L., Eleni Ravanis, S., McEwen, A., Thomas, N., Hayne, P., Seelos, K., Shane Byrne, A., Roth, M., Martin Philippe Sarrazin, L., Corbin Kling, S., 2021. Mid-Latitude Ice on Mars: A Science Target for Planetary Climate Histories and an Exploration Target for In Situ Resources. Bull. AAS 53. https://doi.org/10.3847/25C2CFEB.CC90422D

Bramson, A.M., Byrne, S., Putzig, N.E., Sutton, S., Plaut, J.J., Brothers, T.C., Holt, J.W., 2015. Widespread excess ice in Arcadia Planitia, Mars. Geophys. Res. Lett. 42, 6566–6574. https://doi.org/10.1002/2015GL064844

Bramson, D.A., Petersen, D.E., 2020. Subsurface Water Ice Mapping [WWW Document]. SWIM. URL https://swim.psi.edu/radar.php (accessed 10.11.21).

Brough, S., Hubbard, B., Hubbard, A., 2019. Area and volume of mid-latitude glacier-like forms on Mars. Earth Planet. Sci. Lett. 507, 10–20. https://doi.org/10.1016/J.EPSL.2018.11.031

Campbell, B.A., 2014. U . S . Shallow Radar (Sharad) Data Product. NASA PDS Doc.

Campbell, B.A., Morgan, G.A., 2018. Fine-Scale Layering of Mars Polar Deposits and Signatures of Ice Content in Nonpolar Material From Multiband SHARAD Data Processing. Geophys. Res. Lett. 45, 1759–1766. https://doi.org/10.1002/2017GL075844

Campbell, B.A., Phillips, R., Putzig, N., 2006. PDS: Data Set Information.

Campbell, B.A., Putzig, N.E., Carter, L.M., Morgan, G.A., Phillips, R.J., Plaut, J.J., 2013. Roughness and near-surface density of Mars from SHARAD radar echoes. J. Geophys. Res. Planets 118, 436–450. https://doi.org/10.1002/JGRE.20050

Conway, S.J., Butcher, F.E.G., de Haas, T., Deijns, A.A.J., Grindrod, P.M., Davis, J.M., 2018. Glacial and gully erosion on Mars: A terrestrial perspective. Geomorphology. https://doi.org/10.1016/j.geomorph.2018.05.019

Degenhardt, J.J., Giardino, J.R., 2003. Subsurface investigation of a rock glacier using ground-penetrating radar: Implications for locating stored water on Mars. J. Geophys. Res 108, 8036. https://doi.org/10.1029/2002JE001888

Dickson, J.L., Head, J.W., Marchant, D.R., 2008. Late Amazonian glaciation at the dichotomy boundary on Mars: Evidence for glacial thickness maxima and multiple glacial phases. Geology 36, 411–414. https://doi.org/10.1130/G24382A.1

Dundas, C.M., Bramson, A.M., Ojha, L., Wray, J.J., Mellon, M.T., Byrne, S., McEwen, A.S., Putzig, N.E., Viola, D., Sutton, S., Clark, E., Holt, J.W., 2018. Exposed subsurface ice sheets in the Martian mid-latitudes. Science (80-.). 359, 199–201. https://doi.org/10.1126/SCIENCE.AAO1619

Fastook, J.L., Head, J.W., Marchant, D.R., 2014. Formation of lobate debris aprons on Mars: Assessment of regional ice sheet collapse and debris-cover armoring. Icarus 228, 54–63. https://doi.org/10.1016/j.icarus.2013.09.025

Gupta, V., Gupta, S.K., Kim, J., 2020. Automated Discontinuity Detection and Reconstruction in Subsurface Environment of Mars Using Deep Learning: A Case Study of SHARAD Observation. Appl. Sci. 2020, Vol. 10, Page 2279 10, 2279. https://doi.org/10.3390/APP10072279

Head, J.W., Marchant, D.R., Agnew, M.C., Fassett, C.I., Kreslavsky, M.A., 2006. Extensive valley glacier deposits in the northern mid-latitudes of Mars: Evidence for Late Amazonian obliquity-driven climate change. Earth Planet. Sci. Lett. 241, 663–671. https://doi.org/10.1016/J.EPSL.2005.11.016

Head, J.W., Marchant, D.R., Dickson, J.L., Kress, A.M., Baker, D.M., 2010. Northern mid-latitude glaciation in the Late Amazonian period of Mars: Criteria for the recognition of debris-covered glacier and valley glacier landsystem deposits. Earth Planet. Sci. Lett. 294, 306–320. https://doi.org/10.1016/J.EPSL.2009.06.041

Head, J.W., Mustard, J.F., Kreslavsky, M.A., Milliken, R.E., Marchant, D.R., 2003. Recent ice ages on Mars. Nature 426, 797–802. https://doi.org/10.1038/nature02114

Head, J.W., Neukum, G., Jaumann, R., Hiesinger, H., Hauber, E., Carr, M., Masson, P., Foing, B., Hoffmann, H., Kreslavsky, M., Werner, S., Milkovich, S., Van Gasselt, S., 2005. Tropical to mid-latitude snow and ice accumulation, flow and glaciation on Mars. Nature 434, 346–351. https://doi.org/10.1038/nature03359

Hepburn, A. J., Ng, F.S.L., Livingstone, S.J., Holt, T.O., Hubbard, B., 2020. Polyphase Mid-Latitude Glaciation on Mars: Chronology of the Formation of Superposed Glacier-Like Forms from Crater-Count Dating. J. Geophys. Res. Planets 125, e2019JE006102. https://doi.org/10.1029/2019JE006102

Hepburn, A. J., Ng, F.S.L., Livingstone, S.J., Holt, T.O., Hubbard, B., 2020. Polyphase Mid-Latitude Glaciation on Mars: Chronology of the Formation of Superposed Glacier-Like Forms from Crater-Count Dating. J. Geophys. Res. Planets 125, e2019JE006102. https://doi.org/10.1029/2019JE006102

Holt, J.W., Safaeinili, A., Plaut, J.J., Head, J.W., Phillips, R.J., Seu, R., Kempf, S.D., Choudhary, P., Young, D.A., Putzig, N.E., Biccari, D., Gim, Y., 2008. Radar sounding evidence for buried glaciers in the southern mid-latitudes of Mars. Science (80-.). 322, 1235–1238. https://doi.org/10.1126/science.1164246

Karlsson, N.B., Schmidt, L.S., Hvidberg, C.S., 2015. Volume of Martian midlatitude glaciers from radar observations and ice flow modeling. Geophys. Res. Lett. 42, 2627–2633. https://doi.org/10.1002/2015GL063219

Lalich, D.E., Holt, J.W., Smith, I.B., 2019. Radar Reflectivity as a Proxy for the Dust Content of Individual Layers in the Martian North Polar Layered Deposits. J. Geophys. Res. Planets 124, 1690–1703. https://doi.org/10.1029/2018JE005787

Levy, J.S., Fassett, C.I., Head, J.W., Schwartz, C., Watters, J.L., 2014. Sequestered glacial ice contribution to the global Martian water budget: Geometric constraints on the volume of remnant, midlatitude debris-covered glaciers. J. Geophys. Res. Planets 119, 2188–2196. https://doi.org/10.1002/2014JE004685

Levy, J.S., Head, J.W., Marchant, D.R., 2007. Lineated valley fill and lobate debris apron stratigraphy in Nilosyrtis Mensae, Mars: Evidence for phases of glacial modification of the dichotomy boundary. J. Geophys. Res. Planets 112, 8004. https://doi.org/10.1029/2006JE002852

Milliken, R.E., Mustard, J.F., Goldsby, D.L., 2003. Viscous flow features on the surface of Mars: Observations from high-resolution Mars Orbiter Camera (MOC) images. J. Geophys. Res. Planets 108, 5057. https://doi.org/10.1029/2002JE002005

Mischna, M.A., Richardson, M.I., Wilson, R.J., McCleese, D.J., 2003. On the orbital forcing of Martian water and CO2 cycles: A general circulation model study with simplified volatile schemes. J. Geophys. Res. E Planets 108, 5062. https://doi.org/10.1029/2003je002051

Mishra, S.K., Bharti, R.R., 2020. Physics News Subsurface detections by SHAllow RADar (SHARAD) on MARS.

Morgan, G.A., Head, J.W., Marchant, D.R., 2009. Lineated valley fill (LVF) and lobate debris aprons (LDA) in the Deuteronilus Mensae northern dichotomy boundary region, Mars: Constraints on the extent, age and episodicity of Amazonian glacial events. Icarus 202, 22–38. https://doi.org/10.1016/J.ICARUS.2009.02.017

Morgan, G.A., Putzig, N.E., Perry, M.R., Sizemore, H.G., Bramson, A.M., Petersen, E.I., Bain, Z.M., Baker, D.M.H., Mastrogiuseppe, M., Hoover, R.H., Smith, I.B., Pathare, A., Dundas, C.M., Campbell, B.A., 2021. Availability of subsurface water-ice resources in the northern mid-latitudes of Mars. Nat. Astron. https://doi.org/10.1038/s41550-020-01290-z

Murchie, S., 2010. Mars Reconnaissance Orbiter Compact Reconnaissance Imaging Spectrometer for Mars Limb Data Record, MRO-M-CRISM-6-LDR-V1.0 [WWW Document]. NASA Planet. Data Syst. URL https://pds.nasa.gov/ds-view/pds/viewProfile.jsp?dsid=MRO-M-CRISM-6-LDR-V1.0 (accessed 6.23.22).

Murchie, S., Arvidson, R., Bedini, P., Beisser, K., Bibring, J.P., Bishop, J., Boldt, J., Cavender, P., Choo, T., Clancy, R.T., Darlington, E.H., Des Marais, D., Espiritu, R., Fort, D., Green, R., Guinness, E., Hayes, J., Hash, C., Heffernan, K., Hemmler, J., Heyler, G., Humm, D., Hutcheson, J., Izenberg, N., Lee, R., Lees, J., Lohr, D., Malaret, E., Martin, T., McGovern, J.A., McGuire, P., Morris, R., Mustard, J., Pelkey, S., Rhodes, E., Robinson, M., Roush, T., Schaefer, E., Seagrave, G., Seelos, F., Silverglate, P., Slavney, S., Smith, M., Shyong, W.J., Strohbehn, K., Taylor, H., Thompson, P., Tossman, B., Wirzburger, M., Wolff, M., 2007. Compact Connaissance Imaging Spectrometer for Mars (CRISM) on Mars Reconnaissance Orbiter (MRO). J. Geophys. Res. E Planets 112. https://doi.org/10.1029/2006JE002682

Nazari-Sharabian, M., Aghababaei, M., Karakouzian, M., Karami, M., 2020. Water on Mars—A Literature Review. Galaxies 2020, Vol. 8, Page 40 8, 40. https://doi.org/10.3390/GALAXIES8020040

Pan, L., Ehlmann, B.L., 2018. Aqueous Processes From Diverse Hydrous Minerals in the Vicinity of Amazonian-Aged Lyot Crater. J. Geophys. Res. Planets 123, 1618–1648. https://doi.org/10.1029/2017JE005461

Parsons, R., Holt, J., 2016. Constraints on the formation and properties of a Martian lobate debris apron: Insights from high-resolution topography, SHARAD radar data, and a numerical ice flow model. J. Geophys. Res. E Planets. https://doi.org/10.1002/2015JE004927

Pauw, L., Hiesinger, H., Hauber, E., 2022. Geological Mapping of the Deuteronilus Mensae region of Mars; Implications for Glacial and Fluvial processes [WWW Document]. URL https://lpsc2022.ipostersessions.com/default.aspx?s=90-01-B8-D5-84-59-9D-3C-9E-DE-35-C3-23-F2-0E-07&guestview=true (accessed 6.20.22).

Petersen, E.I., Holt, J.W., Levy, J.S., 2018. High Ice Purity of Martian Lobate Debris Aprons at the Regional Scale: Evidence from an Orbital Radar Sounding Survey in Deuteronilus and Protonilus Mensae. Geophys. Res. Lett. 45, 11,595-11,604. https://doi.org/10.1029/2018GL079759

Picardi, G., Plaut, J.J., Biccari, D., Bombaci, O., Calabrese, D., Cartacci, M., Cicchetti, A., Clifford, S.M., Edenhofer, P., Farrell, W.M., Federico, C., Frigeri, A., Gurnett, D.A., Hagfors, T., Heggy, E., Herique, A., Huff, R.L., Ivanov, A.B., Johnson, W.T.K., Jordan, R.L., Kirchner, D.L., Kofman, W., Leuschen, C.J., Nielsen, E., Orosei, R., Pettinelli, E., Phillips, R.J., Plettemeier, D., Safaeinili, A., Seu, R., Stofan, E.R., Vannaroni, G., Watters, T.R., Zampolini, E., 2005. Planetary science: Radar soundings of the subsurface of Mars. Science (80-.). 310, 1925–1928. https://doi.org/10.1126/SCIENCE.1122165/ASSET/778E1353-203F-415F-A790-44039EF6547F/ASSETS/GRAPHIC/310_1925_F4.JPEG

Plaut, J J, Holt, J.W., Head, J.W., Gim, Y., Choudhary, P., Baker, D.M., Kress, A., 2009. Thick Ice Deposits in Deuteronilus Mensae, Mars: Regional Distribution from Radar Sounding.

Plaut, Jeffrey J, Safaeinili, Ali, Holt, John W, Phillips, Roger J, Head III, James W, Seu, Roberto, Putzig, Nathaniel E, Frigeri, Alessandro, Safaeinili, A, Holt, J W, Phillips, R J, Head III, J W, Seu, R, Putzig, N E, Frigeri, A, 2009. Radar evidence for ice in lobate debris aprons in the mid-northern latitudes of Mars. Geophys. Res. Lett. 36. https://doi.org/10.1029/2008GL036379

PSI, 2020. NASA PORPASS Project | Planetary Science Institute [WWW Document]. Planet. Sci. Inst. News. URL https://www.psi.edu/news/porpass (accessed 6.25.22).

Putzig, N., 2014. CPB : The CO-SHARPS Processing Boutique SHARAD Processors. SHARAD/MARSIS Data Users' Work. 30.

Seu, R., Biccari, D., Orosei, R., Lorenzoni, L. V., Phillips, R.J., Marinangeli, L., Picardi, G., Masdea, A., Zampolini, E., 2004. SHARAD: The MRO 2005 shallow radar. Planet. Space Sci. 52, 157–166. https://doi.org/10.1016/J.PSS.2003.08.024

Seu, R., Phillips, R.J., Biccari, D., Orosei, R., Masdea, A., Picardi, G., Safaeinili, A., Campbell, B.A., Plaut, J.J., Marinangeli, L., Smrekar, S.E., Nunes^, D.C., 2007. SHARAD sounding radar on the Mars Reconnaissance Orbiter. J. Geophys. Res. 112, 5–05. https://doi.org/10.1029/2006JE002745

Smith, E.D., 1999. Mola Initial Experiment Gridded Data Record, Mgs-M-Mola-5-Iegdr-L3-V2.0, [WWW Document]. NASA Planet. Data Syst. URL https://pds.nasa.gov/ds-view/pds/viewProfile.jsp?dsid=MGS-M-MOLA-5-IEGDR-L3-V2.0 (accessed 6.23.22).

Smith, I., Hayne, P.O., Byrne, S., Becerra, P., Kahre, M., Calvin, W., Hvidberg, C., Milkovich, S., Buhler, P., Landis, M., Horgan, B., Kleinböhl, A., Perry, M.R., Obbard, R., Stern, J., Piqueux, S., Thomas, N., Zacny, K., Carter, L., Edgar, L., Emmett, J., Navarro, T., Hanley, J., Koutnik, M., Putzig, N., Henderson, B.L., Holt, J.W., Ehlmann, B., Parra, S., Lalich, D., Hansen, C., Hecht, M., Banfield, D., Herkenhoff, K., Paige, D.A., Skidmore, M., Staehle, R.L., Siegler, M., Soto, A., Foss, F., Lewis, S., Whitten, J., Vos, E., Johnson, P.A., Johnson, J.C., Gallagher, C., Brown, A., Bertrand, T., Phillips-Lander, C., Oliveira, N., Kite, E., Thorsteinsson, T., Tamppari, L., Hauber, E., Fanara, L., Oberst, J., Ulamec, S., Cartwright, S., Harrison, T., Hibbard, S., Portyankina, A., Titus, T.N., 2021. Unlocking the Climate Record Stored within Mars' Polar Layered Deposits. Bull. AAS 53. https://doi.org/10.3847/25C2CFEB.F5EE96DC

Smith, I.B., Putzig, N.E., Holt, J.W., Phillips, R.J., 2016. An ice age recorded in the polar deposits of mars. Science (80-.). 352, 1075–1078. https://doi.org/10.1126/SCIENCE.AAD6968/SUPPL_FILE/SMITH.SM.PDF

Souness, C., Hubbard, B., Milliken, R.E., Quincey, D., 2012. An inventory and population-scale analysis of martian glacier-like forms. Icarus 217, 243–255. https://doi.org/10.1016/j.icarus.2011.10.020

Stuurman, C.M., Osinski, G.R., Holt, J.W., Levy, J.S., Brothers, T.C., Kerrigan, M., Campbell, B.A., 2016. SHARAD detection and characterization of subsurface water ice deposits in Utopia Planitia, Mars. Geophys. Res. Lett. 43, 9484–9491. https://doi.org/10.1002/2016GL070138

Victoria, R., Petrescu, V., Aversa, R., Apicella, A., Kozaitis, S., Abu-Lebdeh, T., Ion, F., Petrescu, T., 2018. There is Life on Mars? Am. J. Eng. Appl. Sci. Orig. Res. 11. https://doi.org/10.3844/ajeassp.2018.78.91

Viviano-Beck, C.E., Seelos, F.P., Murchie, S.L., Kahn, E.G., Seelos, K.D., Taylor, H.W., Taylor, K., Ehlmann, B.L., Wisemann, S.M., Mustard, J.F., Morgan, M.F., 2014. Revised CRISM spectral parameters and summary products based on the currently detected mineral diversity on Mars. J. Geophys. Res. Planets 119, 1403–1431. https://doi.org/10.1002/2014JE004627

Whitten, J.L., Campbell, B.A., Morgan, G.A., 2017. A subsurface depocenter in the South Polar Layered Deposits of Mars. Geophys. Res. Lett. 44, 8188–8195. https://doi.org/10.1002/2017GL074069